DOI: https://doi.org/10.2138/am-2022-8808. http://www.minsocam.org/

Revision 1:

Word Count: 8991

Effect of faceting on olivine wetting properties

Yongsheng Huang[1, a*], Takayuki Nakatani[1, b], Sando Sawa[1], Guoji Wu[2], Michihiko Nakamura[1], Catherine McCammon[3]

Affiliations:

1. Department of Earth Science, Graduate School of Science, Tohoku University, Aramaki-Aza-Aoba, Aoba-Ku, Sendai, Miyagi 980-8578, Japan.
2. College of Earth and Planetary Sciences, University of Chinese Academy of Sciences, 19A Yuquan, Shijingshan, Beijing 100049, China.
3. Bayerisches Geoinstitut, University of Bayreuth, Bayreuth 95440, Germany.

a. Current address: Guangzhou Institute of Geochemistry, Chinese Academy of Sciences, 511 Kehua Street, Wushan, Tianhe, Guangzhou 510640, China.
b. Current address: Geological Survey of Japan, AIST Central 7, Higashi 1-1-1, Tsukuba, Ibaraki 305-8567, Japan.

* Corresponding author. Email: huangyongsheng@gig.ac.cn

Abstract

Grain-scale pore geometry primarily controls the fluid distribution in rocks, affecting material transport and geophysical response. The dihedral angle (θ) in the olivine–fluid system is a key parameter determining pore fluid geometry in mantle wedges. In the system, curved and faceted olivine–fluid interfaces define θ, resulting in faceted–faceted (FF), faceted–curved (FC), and curved–curved (CC) angles. The effect of faceting on θ under various pressure and temperature (P–T) conditions and fluid compositions, however, have not been constrained, and mineralogical understanding remains unresolved. This study evaluated facet-bearing θ and their proportions in olivine–multicomponent aqueous fluid systems. Our results show that 1/3 of olivine–fluid θ are facet-bearing angles, regardless of the P–T conditions and fluid composition. Faceting produces larger dihedral angles than CC angles. The grain boundary plane (GBP) distribution reveals that the GBPs of faceted interfaces at triple junctions have low Miller index faces ({100}, {010}, and {101}). The misorientation angle/axis distributions of adjacent grain pairs are in accord with a theoretical distribution of random olivine aggregate. Moreover, the calculation of the FF angles for adjacent grain pairs with low Miller index GBPs reproduces measured angle values based on the olivine crystal habit. Therefore, our study suggests that the FF angle is strongly affected by olivine crystallography. The presence of faceting increases θ and a critical fluid fraction (ϕ_c) for percolation, lowering permeability. In the mantle wedge, where olivine crystallographic preferred orientation (CPO) is expected owing to corner flow, increasing the FF angle proportion with associated changes in fluid pore morphology will lead to permeability anisotropy, controlling the direction of the fluid flow, and resulting in geophysical anomalies such as seismic wave attenuation and high electrical conductivity.

Keywords: dihedral angle, faceted plane, Miller index, crystallographic orientation, permeability anisotropy, mantle wedge.

1. Introduction

Pore geometry significantly controls the distribution of geological fluids (i.e., aqueous fluids and silicate melt) in deep mantle wedges, thereby affecting element cycling and geophysical responses in subduction zones (Watson and Brenan 1987; Hermann et al. 2006; Iwamori 1998; van Keken et al. 2011; Pommier and Evans 2017; Worzewski et al. 2011; Zheng et al. 2016). Although channelized fluid flow has often been inferred from field studies (Angiboust et al. 2014), pervasive grain-scale fluid flow may be the most plausible fluid migration regime at high pressure (P) and high temperature (T) conditions where dissolution–precipitation intensively operates and interfacial energy minimization ("textural equilibrium") is quickly attained. Moreover, the pervasive nature may be suitable for explaining the resistivity anomalies observed at a magnetotelluric (MT) grid scale (commonly > 10 km) because it would be required for the channelized flows to be distributed continuously and nearly isotropically over this length scale. In an olivine-dominant mantle rock, the olivine–fluid dihedral angle (θ) is the primary parameter controlling grain-scale fluid connectivity (Toramaru and Fujii 1986; Mibe et al. 1999; Huang et al. 2019, 2020). Therefore, a precise constraint on θ in the olivine–fluid system is important for a complete understanding of the fluid distribution and migration in subduction zones.

The dihedral angle is a consequence of the fluid–mineral interaction, which changes the fluid pore geometry through dissolution and precipitation processes to minimize the interfacial energy in the system. It is defined as the ratio of the grain boundary energy (γ_{ss}) to the solid–fluid interfacial energy (γ_{sf}) (Smith 1964) as follows:

$$2\,cos(\theta/2) = \gamma_{ss}/\gamma_{sf} \qquad (1)$$

In an isotropic system where solid–fluid interfaces are smoothly curved with a constant mean curvature; the equilibrium geometry of the intergranular fluid is solely determined by the dihedral angle. In a fluid-bearing rock with a low fluid fraction (ϕ), fluids can wet the grain edges well and migrate along interconnected tubular networks at θ < 60° irrespective of the fluid fraction. On the contrary, at θ > 60°, the fluid is distributed as isolated pockets along the grain edges, corners, and boundaries (Smith 1948; Watson and Brenan 1987; Holness 1992, 1993), although the unstable interconnected network can be transiently formed above the critical fluid fraction (ϕ_c) (Park and Yoon 1985; von Bargen and Waff 1986; Laporte and Provost 2000). However, the fluid distribution in realistic rocks can deviate from the ideal distribution (Waff and Faul 1992; Laporte and Watson 1995). Huang et al. (2021) measured the electrical conductivity of a texturally equilibrated forsterite–saline fluid aggregate at 800°C and 1 GPa and showed that the conductivity was significantly smaller than that expected from the interconnected tube model, especially at low ϕ. The synchrotron X-ray microtomography (CT) of the post-run products revealed that fluid pores struggled to become interconnected at ϕ approximately <1.0% even though θ defined by the curved–curved interface was < 60° under the experimental conditions (Huang et al. 2019).

In a realistic mineral–fluid system with interfacial energy anisotropy, facet planes (i.e., crystallographically controlled planar solid–liquid interfaces) are often present along with curved interfaces (Waff and Faul 1992; Watson and Lupulescu 1993; Cmíral et al. 1998; Watson 1999; Wark and Watson 2000; Price et al. 2006). A curved interface results from a constant mean curvature that minimizes the surface energy by minimizing the surface area (Bargen and Waff 1986; Waff and Faul 1992), whereas a flat interface is attributed to crystallographically controlled minimum interfacial energy (Yoshino et al. 2006). The coexistence of both curved and faceted interfaces generates three types of θ: curved–curved (CC), faceted–curved (FC), and faceted–faceted (FF) (Price et al. 2006; Yoshino et al. 2006). Pores surrounded by facet planes are difficult to connect unless the fluid/melt fraction exceeds a critical value, which depends on θ defined by the faceted interfaces (Waff and Faul 1992; Cmíral et al. 1998; Price et al. 2006). Therefore, the facet plane may affect the fluid connectivity depending on its θ values, which helps to explain the results of electrical conductivity measurements by Huang et al. (2021). Waff and Faul (1992) and Cmíral et al. (1998) investigated θ in partially molten rock systems and showed that FF angles are larger than FC and CC angles. Price et al. (2006) reported that FF and FC angles are larger than CC angles in the quartz–fluid and tremolite–fluid systems at 900–950 °C and approximately 1.5 GPa. These findings imply that facet-bearing pores necessitate a relatively high ϕ for fluid interconnection.

Although many studies have been conducted to investigate the P–T, fluid composition, and mineral assemblage dependence of θ in the olivine–fluid system (Watson and Brenan 1987; Huang et al. 2019, 2020; Mibe et al. 1998, 1999; Yoshino et al. 2006), the effect of angle type variation on θ is poorly understood. Yoshino et al. (2006) systematically investigated the effect of faceting on pore geometry in texturally equilibrated rocks and discussed its implications for permeability in several representative systems, including the San Carlos olivine–MORB melt. However, olivine (forsterite)–aqueous fluid systems have not yet been studied. Huang et al. (2019, 2020) focused on the CC θ between olivine and multicomponent aqueous fluids over a wide range of pressures and temperatures and proposed that multicomponent fluids derived from the subducting slab can travel through the deep fore-arc mantle wedge and cause electrical conductivity anomalies observed in

This is the peer-reviewed, final accepted version for American Mineralogist, published by the Mineralogical Society of America.
The published version is subject to change. Cite as Authors (Year) Title. American Mineralogist, in press.
DOI: https://doi.org/10.2138/am-2022-8808. http://www.minsocam.org/

various subduction zones. Laporte and Provost (2000) investigated theoretically θ in a system with simplified surface energy anisotropy and found that the relationship between the mean equilibrium θ and the grain boundary to the surface energy ratio was close to the isotropic case. However, few studies have provided empirical evidence for facet-bearing dihedral angles with respect to crystallographic orientations for actual mineral–fluid systems with various fluid compositions.

Investigating the grain boundary plane distribution (GBPD) can provide a mineralogical understanding of angle types in terms of FF, FC, and CC angles. Some researchers have investigated GBPD in fluid-free olivine polycrystals and found that low Miller index planes preferentially appear in the grain boundaries (Faul and Fitz Gerald 1999; Marquardt et al. 2015). If such specific grain boundary planes (GBPs) appear preferentially at the facet-bearing triple junctions in the mineral–fluid system, they may significantly control θ of the facet-bearing angles and their resultant fluid pore geometry. However, previous studies did not distinguish the grain boundary type in terms of angle type (i.e., FF, FC, or CC), and GBPD has not been examined in fluid-bearing systems.

In this study, we investigated the facet-bearing (i.e., FF and FC) θ in the run products of olivine–fluid systems previously obtained by piston-cylinder experiments at various pressures (P: 1–3 GPa), temperatures (T: 800–1100 °C), and fluid compositions (pure H_2O, H_2O–NaCl, and H_2O–CO_2 systems) (Huang et al. 2019, 2020). These experiments broadly covered the P–T conditions and fluid compositions expected in a deep fore-arc mantle wedge. The results were compared with CC θ measured in previous studies to clarify the effect of faceting. Moreover, we examined the crystallographic orientation of the olivine aggregate and identified the GBPD at triple junctions with different angle types to evaluate the influence of crystallographic orientation on θ. Based on the results, we discussed the origin of faceting and its effect on θ and inferred the consequences of faceting on fluid connectivity, fluid distribution, and permeability anisotropy in the olivine–fluid system under static and sheared mantle conditions.

2. Methods

2.1. Samples

We analyzed the run products of olivine–fluid systems previously obtained by Huang et al. (2020, 2019). To constrain the P–T and fluid composition dependency of the facet-bearing θ, we selected 19 samples that covered a wide range of experimental P–T conditions (1–3 GPa and 800–1100 °C) and fluid compositions (H_2O, H_2O–CO_2 with $X_{(CO2)} = CO_2/(H_2O+CO_2) = 0.5$ in molar ratio), and H_2O–NaCl with 5.0 and 27.5 wt.% NaCl). Run products containing magnesite and orthopyroxene due to olivine carbonation (Huang et al., 2020) were excluded to avoid the effect of mineral species other than olivine.

Experimental procedures to synthesize the samples followed those of previous studies (Huang et al., 2020, 2019) and are briefly described here. High P–T experiments were conducted at Bayerisches Geoinstitut, University of Bayreuth, using end-loaded piston-cylinder apparatus. Piston diameters of 3/4 inch and 1/2 inch were used for experiments at pressures of 1–2 GPa and 3 GPa, respectively, along with a standard Talc–Pyrex assembly (Keppler et al. 2003). The starting material was San Carlos olivine powder ($Fo_{91}Fa_9$) with a grain size of 38–53 μm. Deionized and distilled water were used as pure H_2O sources. Pure oxalic acid dihydrate ($C_2H_2O_4 \cdot 2H_2O$) was used as the CO_2 source. To obtain the NaCl solution, we dissolved reagent-grade NaCl (99.99% NaCl) in deionized and distilled water at room temperature (approximately 25°C) and atmospheric pressure. Water and hydrous oxalic acid were mixed to obtain the target $X_{(CO2)}$. The olivine powder, combined with approximately 10.0 vol.% fluid, was loaded into an end-welded noble metal capsule that was sealed by arc welding. Au capsules (2.2 mm outer diameter) and $Au_{80}Pd_{20}$ alloy capsules (2.0 mm outer diameter) were used for experiments at 800–1000 °C and 1100°C, respectively. Detailed procedures for the high P–T experiments are shown by Huang et al. (2019, 2020). Briefly, the run duration ranged from 72 to 211 h, depending on the target temperature. The experimental conditions and results are summarized in Table 1. In our experiments, CO_2 was assumed to be the predominant C species based on previous studies (Allen 1972; Huang et al. 2020; Médard et al. 2008).

The post-run capsules were cut using a diamond wire saw to expose the run products. The run products were then impregnated with epoxy resin under a vacuum. We first polished these products using sandpaper and diamond paste with particle sizes down to 1.0 μm and then using a 0.06 μm colloidal silica suspension. For electron backscattered diffraction (EBSD) analysis, the samples were polished with colloidal silica suspension for more than 10 h using an automatic vibratory polishing machine (VibroMet, Buehler Ltd.).

2.2. Scanning electron microscopy

We observed polished cross-sections of the run charges using a field-emission scanning electron microscope (FE–SEM; JSM–7100F, JEOL Ltd.) with an accelerating voltage of 15 keV. The mineral phases and microstructures of samples were observed. We took FF and FC-type triple junctions for quantitative analysis. More than 300 backscattered electron (BSE) or secondary electron (SE) images of 1280 × 960 pixels were obtained for each run product with high magnifications and resolution, depending on the pore size.

2.3. Dihedral angle measurement

The apparent FF and FC θ were measured at triple junctions on the SEM images using the Image J software (National Institute of Health). We followed the method used for the CC angle measurements by Huang et al. (2019, 2020). The median of measured angles from a two-dimensional (2D) section is likely to be close to the median value of the population of the true three-dimensional (3D) angle (e.g., Harker and Parker 1945; Jurewicz and Jurewicz 1986). Generally, the median of measured angles is close to the 3D median θ value to the greatest extent when a sufficient number of angles are measured by using high magnification and high-resolution SEM images. However, a deviation between the estimated and true angle can occur when the sample suffers from severe plucking during cutting and polishing, which locally reduces the randomness of the apparent angle distribution. Although Cmíral et al. (1998) demonstrated that θ values obtained with transmission electron microscopy (TEM) are smaller than those measured from low magnification SEM images, our FE–SEM images were taken at high magnification (up to 150,000) and provided clear images comparable with those from TEM. In this study, more than 100 angles were measured on the acquired SE images for each angle type for each sample. The statistical error of the median value was estimated to be $< 1.5°$, as discussed by Huang et al. (2020). The details of θ selection and measurement are given by Huang et al. (2019).

2.4. Electron backscattered diffraction

To identify the crystallographic orientation of the olivine aggregate and its consequences on θ, we mapped 10 representative samples using an FE–SEM equipped with an electron backscatter diffractometer (EBSD; HKL Channel5, Oxford Instruments plc.) at Tohoku University. Analyses were conducted at an accelerating voltage of 15.0 kV. We used six Kikuchi reflectors for EBSD analysis, and EBSD mapping was performed using a 250 nm step size. Two types of EBSD data were collected for each sample. Lower magnification (× 200–500) data were collected to investigate the crystallographic preferred orientation (CPO) of the entire sample, while higher magnification (× 5,000–15,000) data were collected to identify crystallographic orientations near the fluid pool. EBSD data were processed using the MTEX MATLAB toolbox.

The degree of mismatch between measured Kikuchi patterns and calculated patterns expected for a given crystal structure is expressed as the mean angular deviation (MAD) value; a higher MAD value is likely to have large uncertainties in measurements. In this study, orientation data with MAD values of > 1.0° were removed, and grain boundaries were detected using a threshold misorientation angle of 10°. Indexed grains smaller than 1 μm were removed during the denoising procedure because they may be caused by mis-indexing. The CPO of analyzed samples were constructed from one point per grain. The index procedure was performed according to the manual of the MTEX MATLAB toolbox. For samples selected for EBSD analysis, we measured the grain size on high resolution SEM images using Image J and normalized grain size using the mean size value.

3. Results

3.1. Product phases and microstructures

In all systems, the recovered samples were composed of olivine aggregates and intergranular fluid pores that were mostly filled with epoxy resin (Figure 1). The grain size of olivine in the run products increased with increasing temperature, reaching approximately 110 μm at 1100°C through grain growth by Ostwald ripening and coalescence of two adjacent grains. The mean grain size of EBSD-analyzed samples ranged from 8.2 to 32.3 μm (Figure 1 and Figure S1 of the Supporting Information). Olivine grains were compositionally homogeneous and fluid-filled pores were generally encompassed by three or more grains. Curved interfaces often coexisted with flat interfaces, even within a single pore (Figure 1). These two kinds of interfaces produced the three types of apparent θ: CC, FC, and FF (Figure 1b, d, and f). The attainment of local interfacial energy minimization via balancing of interfacial tensions at triple junctions (i.e., textural equilibration) was demonstrated by (1) the occurrence of many olivine–olivine–olivine triple junctions with angles of approximately 120° (Figure 1a, e; e.g., Liu et al., 2018), (2) cumulative frequency curves for apparent θ that showed good agreement with the predicted curve for an equilibrated texture (Harker and Parker 1945; Elliott et al. 1997), and (3) a normalized grain size distribution concentrated on the mean grain size (Figure 1g, h; Figure S1 of the Supporting Information; Faul 1997; Huang et al. 2021). This is supported by the fact that the experimental durations (72–211 h) were sufficiently long for attaining textural equilibrium compared with those in previous studies (e.g., 12 h for a grain size of 10 μm at 727°C, Holness and Siklos 2000). Once texture equilibrium is attained in the system, true 3D θ likely remains constant with normal grain growth. We measured the apparent FF and FC angles with clear interfaces (e.g., angles denoted by green rectangles in Figure 1b) and excluded those affected by cracks (e.g., the angle indicated by the red rectangle in Figure 1d).

3.2. Proportion of faceting-bearing angles

The proportion of facet-bearing angles (i.e., FF and FC angles) was evaluated from the SEM images of each recovered sample using Image J (Figure 2). A total of 5,025 angles were counted from the 19 samples (Table 1). To avoid the potential effect of heterogeneity in the angle type distribution, we processed several images and obtained an average value for each sample.

Although minor fluctuations occurred, the facet-bearing angle proportion was almost constant at approximately 32.5% (± 0.5) without systematic P–T and fluid composition dependencies. Namely, the FF and FC angles constituted approximately 1/3 of the dihedral angles. It is well demonstrated that the proportion of faceting is primarily controlled by ϕ and that the faceting proportion increases with an increase in the liquid fraction in the solid–liquid system because of increases in lower surficial energy planes induced by grain rotation at high ϕ. (Watson and Lupulescu 1993; Wark and Watson 2000; Watson 1999; Yoshino et al. 2005, 2006). Yoshino et al. (2005, 2006) reported that the faceting interface fraction in the olivine–basaltic melt system mostly fell in the range of 30.0–35.0% with a melt fraction of 10.1–16.5 vol.%. Given an initial ϕ of approximately 10.0 vol.% in our study, our calculated faceting proportion was roughly consistent with the previous research (Yoshino et al. 2006). Although the amount of faceting can be affected by surface adsorption, which is a function of fluid compositions (Kretz 1966), the fluid composition dependence of the proportion of facet-bearing angles was not obvious in our run products.

3.3. Cumulative frequency of apparent dihedral angles

Representative cumulative frequencies of the measured FF and FC angles in the olivine–fluid systems at 2 GPa are shown in Figure 3; curves of the apparent CC angles from Huang et al. (2019, 2020) are plotted for comparison. Cumulative frequencies for the other conditions and histograms for all systems in this study are shown in Figure S2 and Figure S3 of the Supporting Information. For all systems investigated, the cumulative frequencies mostly showed a sharp increase around the median θ, and the frequency distribution histogram also showed a concentrated distribution of measured angles around the median value. In most cases, the cumulative frequency of CC angles sharply increased around the median θ, which is in accord with the theoretical prediction for the isotropic system with one true θ. In contrast, the cumulative frequency of FF angles gradually increased around the median angle, which we attributed to an expanded range of true 3D angles owing to the anisotropy of interfacial energy which acts to rotate interfaces into the lowest energy orientation (Laporte and Provost 2000). In some cases (Figure 3), the cumulative frequency of FF and FC θ largely deviated from the theoretical curve in regions of high apparent θ. This deviation was, first, attributed to the relatively small number of measured apparent FF angles. However, it can also be attributed to the presence of a very large θ, possibly associated with sub-grain boundaries, in which the misorientation angle between two adjacent grains is very small (Laporte et al. 1997). These two possible reasons caused the cumulative frequency of FF and FC angles to deviate far from the theoretical prediction compared with that of the CC angle. Nevertheless, the median angles in such cases were assumed to represent the true 3D value most frequently occurring in the system because angles smaller than the median fit the theoretical line well.

3.4. Faceting effect on the median dihedral angle

The angle type dependence of the median θ in the olivine–fluid systems at 1–3 GPa and 800–1100 °C is shown in Figure 4. We classified the experimental systems into two groups (I group: independent angle type; D group: dependent angle type) based on whether the angle type effect was prominent or not. The angle values were comparable among the CC, FC, and FF in the H_2O system at relatively low P–T conditions and in the H_2O–CO_2 system (I group). In contrast, the median angle of the facet-bearing angles was higher than that of the CC angle in the H_2O system under higher P–T conditions and in the H_2O–NaCl system (D group). The corresponding groups for each run product are summarized in Table 1. The duration of experiments in both the I and D groups was sufficiently long for dihedral angle equilibration, and disequilibrium could not cause their differences. Under constant P–T conditions, FC and CC angles showed a relatively wide variation in θ between the H_2O and H_2O–NaCl systems, except for the results at 3 GPa and 1100°C, for which the difference almost disappeared. In contrast, the variation of FF θ was generally limited among the different fluid systems, with a few exceptions in the H_2O–CO_2 and H_2O–NaCl (5.0 wt.% NaCl) systems. The three types of θ in the H_2O–CO_2 system at 1 GPa and 1000°C were larger than those of the other fluid compositions. In the H_2O–NaCl (5.0 wt.% NaCl) system, the θ values of the FF angle were similar (Figure 4) or smaller by 5°–10° than those in the H_2O and H_2O–NaCl (27.5 wt.% NaCl) systems at the same P–T conditions (Figure 4d and f).

3.5. P–T dependence of median dihedral angles in different fluid systems

The P–T dependencies of the median FF and FC angles in the olivine–fluid systems measured in this study are shown in Figure 5, along with the CC angles reported by Huang et al. (2019). CC angles decrease with increasing P and T (Figure 5c, f, and i), possibly corresponding to the increase in olivine solubility and enhanced adsorption of fluid components on the olivine surface under high P–T conditions (e.g., Holness 1993; Huang et al. 2019). In contrast, the P–T dependence of the FC and FF angles was not obvious compared to that of the CC angle. In particular, the FF angles showed a stepwise change in θ but had similar θ values (Figure 5a, d, and g). These findings suggest that factors other than solubility variation control θ of FF angles (see Section 4.1 for a more detailed discussion based on EBSD results). It is worth noting that the median values of the FF angle were larger than, or close to, 60° in most cases.

3.6. Crystallographic orientation of olivine

Figure 6 shows the representative EBSD maps and pole figures obtained from the five recovered samples. Figure S4 of the Supporting Information shows the remaining maps and pole figures. Our samples exhibited a weak (010) CPO (i.e., *b* axis slightly parallel to the compression direction of piston cylinder), regardless of the P–T conditions or fluid composition. It was not as intense as the strong CPO that developed in the deformed olivine aggregate (Pommier et al. 2018). The weak CPO in this study is reasonable because the cell assembly of the piston cylinder experiments with materials softened at high P–T conditions have been developed to avoid intense differential stress. Figure 7 shows olivine grains' high-magnification orientation maps and the corresponding SE images. Further analyses of the crystallographic orientations of the GBPs are described in Section 4 (Discussion).

3.7. GBP distribution and misorientation angles and axes

To clarify the crystallographic orientation of olivine on GBPs, we evaluated the GBPD for the grain boundaries of the FF, FC, and CC angles on a high-magnification orientation map (Figure 7). In general, GBPs were not always vertical but tended to incline at various degrees with respect to the polished cross-section of the sample. In the 2D SEM images, we could not identify the degree of incline for these planes. In previous studies, GBPD was examined by analyzing the large number of automatically detected grain boundaries in dry polycrystalline systems, and frequently appearing planes were detected after statistical treatment (Marquardt and Faul 2018). In our study, the number of measurements was limited because discrimination of angle types requires a careful observation of each olivine–fluid–olivine triple junction in a high magnification image. To better constrain the GBPD with a limited number of measurements, we focused on olivine–fluid–olivine triple junctions with apparent dihedral angles lower than the median value + 5°, and assumed that their grain boundaries were subvertical to the polished section. For example, in the system with one true θ of 60°, 71% of the apparent dihedral angles fell within the range from 0 to 65°, in which 68% of GBPs formed an angle of ≥ 67° with respect to the sectioning plane. Thus, we inferred representative errors of approximately 23° in our GBPD analyses, although this is a minimum estimate in a simplified system. Without this dihedral angle constraint, the estimated error is 35°. More details about the errors of the GBPD analyses are provided in Supporting Information Note 1 and Figures S5–S6. At such triple junctions, we determined the crystallographic orientations of olivine sharing the assumed vertical GBPs in the nine samples, including both the I and D groups. The relationship between the two touching crystal planes was not examined in this study. In the calculation, we used Euler angles derived from the EBSD analysis and the trend of the GBPs with respect to the horizontal side of the corresponding SEM image. The symmetrically equivalent olivine orientations obtained for each angle type were stereologically projected in the crystal reference frame, as shown in Figure 8. Therefore, the number of geometrically different crystal planes in our analysis can be 16 (= 4^2) with an assumed angle interval of 22.5° (= 90°/4), which is equivalent to our representative GBPD error, for the azimuth and elevation angles in the stereological projection. More than approximately 75 measurements were required to obtain stable GBPD results.

In the I group, low Miller index planes such as {100} and {010} were dominant at grain boundaries of the FF triple junctions, whereas the GBPs of the CC triple junctions were often characterized by a higher Miller index such as {203}. Note that the multiples of uniform density (MUD) spots indexed as {101} and {100} in Figure 8a1 are indistinguishable because of the tilt of the GBP. In the D group, the GBPs of the FF triple junctions were focused on {010} and {130}, which was interpreted as a broad concentration around {010}, and weakly focused on {110}. Although the differences in these planes exceeded the possible errors of approximately ± 20° in our analyses, the large variation in true θ of the FF angles, especially in the D groups (Figure 3b, c, e, f; Section 3.3), could cause the apparent broadening of the concentration around {010} beyond the assumed errors. At the CC triple junctions, high Miller index planes were dominant, and the {100} was relatively weak. The GBPD at the FC triple junctions tended to exhibit mixed characteristics of the FF and CC results in both groups. Although the amount of the data was reduced, the GBPs at the faceted and curved sides were separately analyzed at the FC triple junctions, as shown in Figure 9. As in the FF and CC junctions, the GBPs at the faceted side of FC junctions were dominated by low Miller index planes such as {101}, {010}, and {110}, whereas the GBPs at the curved side of FC junctions preferred high Miller index planes such as {320} and {151}. This indicates that the GBPDs observed in the FF and CC triple junctions are likely true. The weak CPO developed in the run products did not significantly affect the results.

Marquardt et al. (2015) found that fluid-free olivine aggregates have a preferred {100} plane of the grain boundary, which is different from the preferential appearance of the {100}, {010}, and {101} planes on the grain boundaries at the FF angle in the present study. This discrepancy is most likely caused by the high ϕ and various fluid compositions used in our study, and supports the hypothesis that GBPD might be affected by the low fractions of melt, and/or contiguity and composition of the melt (Marquardt and Faul 2018). The crystal habit of olivine grown freely in a fluid-rich system is characterized by the dominant {010} plane (Waff and Faul 1992). Previous studies have shown that the {010} plane of olivine has the lowest energy, followed by the {100} and {001} planes in fluid/melt systems (Deer et al., 2013; Gurmani et al., 2011; de Leeuw et al., 2000; Watson et al., 1997).

The misorientation angles of two adjacent grains selected for GBPD analysis are shown in Figure 10. The misorientation angles at the FC and CC triple junctions show an asymmetric unimodal distribution with a peak at 90° (Figure 10). This is consistent with the theoretical distribution for randomly distributed orthorhombic crystals (e.g., Mackenzie 1958; Morawiec 2010). The misorientation angle at the FF triple junction shows two maxima at 70° and 90°. In partially molten olivine aggregates, Faul and Fitz Gerald (1999) also found the two maxima at 60° and 90° in the misorientation angle distribution of two touching olivine grains with the melt-free boundary. However, owing to a relatively small amount of data in our misorientation analysis, we considered that the misorientation angle distributions were mostly the same among the three angle types and generally in accord with the random distribution. The misorientation axes distribution at the FF, FC, and CC triple junctions were almost indistinguishable from a perfectly random polycrystal distribution (Figure 11). This was similarly confirmed even when the distributions were re-analyzed for the fraction of the data with misorientation angles around the peaks at 90° and 70° (± 5°).

4. Discussion

To check the minimum number of measurements required to obtain stable GBPD results, we performed a series of random tests with dataset b3 in Figure 8, in which 216 measurements were used to make a contour plot. In this test, 25–150 measurements were randomly selected from the original dataset without duplication, and this was repeated 10 times to obtain 10 individual stereograms. We found that the distribution of high MUD derived from the original dataset (b3 in Figure 8) could be well reproduced within the estimated error margins when the random selection number was ≥ 75 (Figure 12 and Figure S7 of the Supporting Information). In our study, the number of measurements was > 75 in most cases, suggesting the robustness of our GBPD results.

However, for the curved and facet sides of the FC angle in the I-group (a2-1 and a2-2 in Figure 9), the number of measurements was reduced to 40. Random tests with ≤ 50 measurement also often reproduced parts of the high MUD spots seen in the original figure (b3 in Figure 8). Thus, the high MUD spots in the above separate analyses may represent part of the true distribution.

Under high P–T conditions, enhanced olivine solubility significantly decreased the interfacial energy with the fluid, resulting in an obvious P–T dependence of θ for the CC angle (Huang et al. 2019, 2020). The effect of fluid composition was also prominent in the case of the CC angle, reflecting the dependence of interfacial energy on fluid compositions (e.g., Holness 1992, 1993). However, θ of the FF angle was less sensitive to P–T conditions and fluid composition than that of the CC angle, with discrete values. Laporte and Provost (2000) theoretically investigated an anisotropic system and showed that θ of the FF angle was controlled by the crystallographic orientation of two adjacent minerals. The extent of surface adsorption among different crystallographic orientations can vary depending on P–T conditions and fluid composition (Kretz 1966), which may switch the dominant facet planes of olivine and explain the stepwise change of the FF θ value in our study.

In this study, GBPD analyses revealed that low Miller index planes, such as {100}, {010}, and {101}, preferentially appeared at the GBPs of the FF angle (Figure 8 and Figure 9). As the faceted mineral–fluid interfaces appeared to have low Miller indices, the θ value of the FF angle could be estimated from the angles between the GBPs of {100}, {010}, {101}, and the other low Miller index olivine surfaces. To test this inference, we calculated the angles between the GBPs of {100} and {010}, and the interfacial boundary crystal planes (IBCPs; i.e., faceted planes with fluids) of {001}, {011}, {110}, {101}, and {120} appearing in the ideal habit of olivine crystals

(Figure 7e). The calculations were made for asymmetrical configurations in which two touching grains have different crystallographic orientations, allowing the grain boundary to be defined. A weak CPO supports the dominance of these configurations in our run products. Triple junctions at which one extended grain boundary plane acts as one of the mineral–fluid interfaces were considered as an extreme case (Flat face in Table 2). All the calculated configurations are presented in Table 1 of the Supporting Information and angles consistent with the experimentally obtained FF θ (i.e., 50°–55°, 55°–65°, 65°–70°, and 75°–80°) are summarized in Table 2. The calculated candidates cover these experimental values in Table 2. For instance, the measured I type FF θ in the H_2O–CO_2 system at 1 GPa and 1000°C was 79.2°. This may correspond to the calculated dihedral angles of 79.2°, 80.1°, and 81.5°, from an asymmetrical triple junction composed of the $\{100\}_{GB}$–$\{101\}_{IB}$ and $\{010\}_{GB}$–$\{021\}_{IB}$, $\{100\}_{GB}$–$\{110\}_{IB}$ and $\{101\}_{GB}$–$\{120\}_{IB}$, and $\{100\}_{GB}$–$\{101\}_{IB}$ and $\{100\}_{GB}$–$\{120\}_{IB}$, respectively. The misorientation angle and axis distributions at the FF triple junctions are indicative of nearly random alignment of two touching grains, showing that the weak CPO developed in the sample had little effect on the FF angles. The θ value of the FC angle may be controlled by both interfacial energy and crystallographic orientation, resulting in FC angles showing intermediate characteristics between FF and CC angles.

5. Implications

5.1. Consequences of faceting on fluid connectivity in an undeformed olivine–fluid system

Our study demonstrates that approximately 1/3 of dihedral angles in the olivine–fluid system are facet-bearing, irrespective of P–T conditions or fluid composition (Table 1). Fluid pores surrounded by faceted interfaces struggle to connect with each other, even at θ < 60°, which requires a threshold ϕ for the establishment of a fluid network, as in the case for CC angles of >

This is the peer-reviewed, final accepted version for American Mineralogist, published by the Mineralogical Society of America.
The published version is subject to change. Cite as Authors (Year) Title. American Mineralogist, in press.
DOI: https://doi.org/10.2138/am-2022-8808. http://www.minsocam.org/

60° (Price et al. 2006). Thus, a system that includes both curved and faceted interfaces with low ϕ, bulk permeability may be reduced. Huang et al. (2021) measured the electrical conductivity of fluid-bearing forsterite aggregate with various ϕ under textural equilibrium states at 1 GPa and 800°C in the H_2O–NaCl system with 5.0 wt.% NaCl. The electrical conductivity measurements and synchrotron X-ray computed CT imaging of the post-run products showed that fluid pores were not interconnected at ϕ of 0.51 vol.%. In contrast, they started to form the fluid network at ϕ of > 2.14 vol.%. Although the CC angle can be lower than 60° under this experimental P–T condition (Huang et al. 2019), fluid interconnection was not established at ϕ below approximately 1.0–2.0 vol.%. This is most likely be attributable to the presence of a substantial number of faceted interfaces that increase ϕ_c and decreases permeability, as pointed out by Price et al. (2006).

Toramaru and Fujii (1986) examined the melt connectivity in peridotites composed of olivine, clinopyroxene, and orthopyroxene based on a bond percolation model with the melt stability at the grain edges and corners, namely, dihedral angles. They found that the melt was not stable at pyroxene-dominated grain edges and that the interconnection was established when pyroxene modal composition was approximately < 25–20 vol.% when the grain size of olivine and pyroxenes were similar. If we assume that faceting triple junctions hamper fluid interconnection, an analogous discussion will be possible for fluid connectivity in facet-bearing olivine aggregates. Given the slightly higher proportion of faceting triple junctions (28%–36%; Table 1) than the above pyroxene modal composition of Toramaru and Fujii (1986), the electrical conductivity results of Huang et al. (2021), in which the fluid percolation was prohibited at $\phi = 0.51$ vol.% but established at a small critical fraction (2.14 vol.%), seems consistent with the model prediction.

5.2. Preferential appearance of faceted fluid pores in sheared mantle

Our study demonstrates that faceted olivine–fluid interfaces are preferentially accompanied by low Miller index GBPs such as {100}, {010}, and {101}. The extensive occurrence of faceted crystallographic faces in deep-seated rocks can change bulk permeability, elastic, anelastic, and electrical properties (Waff and Faul 1992). Waff and Faul (1992) investigated melt distribution in the texturally equilibrated olivine–melt system and found that the presence of melt film along the pervasive faceted crystal interface significantly reduced θ and increased the permeability of the bulk rock. However, the effect of the faceted interface on pore morphology and permeability obtained from olivine–fluid systems in the present study is different from that of the olivine–melt system. Our results show that grain boundaries associated with the flat interface are dry, and that FF and FC angles are comparable to or larger than CC angles, working against the establishment of fluid connectivity. This effect could be magnified under shear stress, such as within the corner flow of subduction zones. In deformed olivine aggregate with strong CPO, crystal axes (i.e., *a*, *b*, and *c* axes) of olivine grains are aligned in specific directions depending on temperature, olivine water content, and stress state (Jung and Karato 2001; Kneller et al. 2005, 2008; Jung et al. 2006; Karato et al. 2008). In addition, Ferreira et al. (2021) found that deformation not only causes strong CPO, but also increases the proportion of particular grain boundary planes (e.g., {010}). This may lead to low Miller index planes dominating grain boundaries, thereby increasing the proportion of facet-bearing angles in sheared mantle.

Jung and Karato (2001) examined a water-saturated olivine fabric under shear strain and found that the *c* axis was subparallel to the shear direction, and the *b* axis was perpendicular to the shear direction (B-type fabric). Therefore, in a water-rich subduction zone, a B-type fabric is expected, in which the *c* axis is subparallel to the subduction direction and the *b* axis is perpendicular to the plate interface. Liu and Zhao (2017) detected Vp anisotropy in the mantle wedge beneath Japan, supporting the hypothesis that the B-type fabric is dominant in the fore-arc mantle wedge. This type of grain alignment could lead to grain boundaries composed of the {100} and {010} planes parallel to the subduction direction to form abundant FF angles that are comparable to or larger than CC angles, decreasing permeability and electrical conductivity along the subduction direction. That is to say, the presence of faceting may change pore geometry and direction of fluid flow, contributing to anisotropy of permeability. The preferred fluid flux induced by faceting in the subduction zone controls flux melting, anomalies of electrical conductivity, and seismic wave velocity attenuation in subduction systems.

6. Conclusions

In this study, we quantitatively determined the effect of faceting on the olivine–fluid θ in different fluid systems (H_2O, H_2O–CO_2 ($X_{(CO2)}$ = 0.5), H_2O–NaCl (5.0 and 27.5 wt.% NaCl)) at 1–3 GPa and 800–1100 °C. The results show that 1/3 of olivine–fluid θ are faceted plane-bearing angles, regardless of the P–T conditions or fluid composition. Our θ measurements show that in the H_2O systems at relatively low P–T conditions and in the H_2O–CO_2 system, facet-bearing angle values (i.e., FF and FC) are comparable to those of the CC angle. However, in the H_2O system at high P–T conditions and in the H_2O–NaCl system, facet-bearing angle values (i.e., FF and FC) are larger than those of the CC angle. EBSD analyses show that the run products did not have an intense CPO corresponding to static compression conditions. Strikingly, the GBPD revealed that faceted and curved interfaces at facet-bearing triple junctions have GBPs with low (e.g., {100}, {010}, {101}) and high (e.g., {130}, {203}, {320}) Miller index faces, respectively. The misorientation angle/axis distributions of adjacent grain pairs were in accord with a theoretical distribution of random olivine aggregate. The calculation of θ values between two adjacent crystal planes strongly reproduced the measured values of the FF angles, which further supports the results of our GBPD analyses. Therefore, our results suggest the importance of crystallographic orientation in determining the origin of the FF angle. The presence of the FF angle and associated changes in fluid pore morphology require a high fluid fraction for establishing fluid networks. This further leads to permeability anisotropy and changes in geophysical characteristics, particularly in mantle wedge settings where olivine CPO is expected.

Acknowledgments

We are grateful to Katharina Marquardt and two anonymous reviewers for their thoughtful reviews and constructive comments. We appreciate Heather Watson for timely editorial handling of this manuscript. We appreciate Xuran Liang for discussing MATLAB. This work was supported by JSPS KAKENHI Grant Nos. JP16H06348 and JP16K13903 awarded to M. Nakamura, JSPS Japanese–German Graduate Externship, International Joint Graduate Program in Earth and Environmental Sciences, Tohoku University (GP–EES), and by the Ministry of Education, Culture, Sports, Science and Technology (MEXT) of Japan under its Earthquake and Volcano Hazards Observation and Research Program, the Core Research Cluster of Disaster Science in Tohoku University (Designated National University), and by the Tuguangchi Award for Excellent Young Scholar (E1510316) in Guangzhou Institute of Geochemistry, Chinese Academy of Sciences. We provide the datasets on figshare (https://doi.org/10.6084/m9.figshare.19786252.v1), including a dataset of pole figures derived from EBSD data and a dataset of FF angle calculation, to support our research.

References

Allen, C.J. (1972) The role of water in the mantle of the earth: the stability of amphiboles and micas. 24th International Geological Congress, Montreal, 2, 231–240.

Angiboust, S., Pettke, T., de Hoog, J.C.M., Caron, B., and Oncken, O. (2014) Channelized Fluid Flow and Eclogite-facies Metasomatism along the Subduction Shear Zone. Journal of Petrology, 55, 883–916.

Cmíral, M., Fitz Gerald, J.D., Faul, U.H., and Green, D.H. (1998) A close look at dihedral angles and melt geometry in olivine-basalt aggregates: A TEM study. Contributions to Mineralogy and Petrology, 130, 336–345.

de Leeuw, N.H., Parker, S.C., Catlow, C.R.A., and Price, G.D. (2000) Modelling the effect of water on the surface structure and stability of forsterite. Physics and Chemistry of Minerals 2000 27:5, 27, 332–341.

Deer et al. (2013) An Introduction to the Rock-Forming Minerals (third edition), 663–664. The Canadian Mineralogist Vol. 51.

Elliott, M.T., Cheadle, M.J., and Jerram, D.A. (1997) On the identification of textural equilibrium in rocks using dihedral angle measurements. Geology, 25, 355–358.

Faul, U.H. (1997) Permeability of partially molten upper mantle rocks from experiments and percolation theory. Journal of Geophysical Research: Solid Earth, 102, 10299–10311.

Faul, U.H., and Fitz Gerald, J.D. (1999) Grain misorientations in partially molten olivine aggregates: an electron backscatter diffraction study. Physics and Chemistry of Minerals 1999 26:3, 26, 187–197.

Ferreira, F., Hansen, L.N., and Marquardt, K. (2021) The effect of grain boundaries on plastic deformation of olivine. Journal of Geophysical Research: Solid Earth, 126(7), e2020JB020273.

Gurmani, S.F., Jahn, S., Brasse, H., and Schilling, F.R. (2011) Atomic scale view on partially molten rocks: Molecular dynamics simulations of melt-wetted olivine grain boundaries. Journal of Geophysical Research: Solid Earth, 116, 12209.

Harker, D., and Parker, E.R. (1945) Grain shape and grain growth. Transactions of the American Society for Metals, 34, 156–201.

Hermann, J., Spandler, C., Hack, A., and Korsakov, A. v. (2006) Aqueous fluids and hydrous melts in high-pressure and ultra-high pressure rocks: Implications for element transfer in subduction zones. Lithos, 92, 399–417.

Holness, M.B. (1992) Equilibrium dihedral angles in the system quartz–CO_2–H_2O–NaCl at 800°C and 1–15 kbar: the effects of pressure and fluid composition on the permeability of quartzites. Earth and Planetary Science Letters, 114, 171–184.

Holness, M.B. (1993) Temperature and pressure dependence of quartz-aqueous fluid dihedral angles: the control of adsorbed H_2O on the permeability of quartzites. Earth and Planetary Science Letters, 117, 363–377.

Holness, M.B., and Siklos, S.T.C. (2000) The rates and extent of textural equilibration in high-temperature fluid-bearing systems. Chemical Geology, 162, 137–153.

Huang, Y., Nakatani, T., Nakamura, M., and McCammon, C. (2019) Saline aqueous fluid circulation in mantle wedge inferred from olivine wetting properties. Nature communications, 10, 5557.

Huang, Y., Nakatani, T., Nakamura, M., and McCammon, C. (2020) Experimental constraint on grain-scale fluid connectivity in subduction zones. Earth and Planetary Science Letters, 552, 116610.

Huang, Y., Guo, H., Nakatani, T., Uesugi, K., Nakamura, M., and Keppler, H. (2021) Electrical Conductivity in Texturally Equilibrated Fluid-Bearing Forsterite Aggregates at 800°C and 1 GPa: Implications for the High Electrical Conductivity Anomalies in Mantle Wedges. Journal of Geophysical Research: Solid Earth, 126, e2020JB021343.

Iwamori, H. (1998) Transportation of H_2O and melting in subduction zones. Earth and Planetary Science Letters, 160, 65–80.

Jung, H., and Karato, S.I. (2001) Water-Induced Fabric Transitions in Olivine. Science, 293, 1460–1463.

Jung, H., Katayama, I., Jiang, Z., Hiraga, T. and Karato, S.I. (2006) Effect of water and stress on the lattice-preferred orientation of olivine. Tectonophysics, 421(1–2), 1–22.

Jurewicz, S.R., and Jurewicz, A.J.G. (1986) Distribution of apparent angles on random sections with emphasis on dihedral angle measurements. Journal of Geophysical Research, 91, 9277.

Karato, S.I., Jung, H., Katayama, I. and Skemer, P. (2008) Geodynamic significance of seismic anisotropy of the upper mantle: New insights from laboratory studies. Annual Review of Earth and Planetary Sciences, 36(1), 59–95.

Keppler, H., Wiedenbeck, M. and Shcheka, S.S. (2003) Carbon solubility in olivine and the mode of carbon storage in the Earth's mantle. Nature, 424(6947), 414–416.

Kneller, E.A., van Keken, P.E., Karato, S.I., and Park, J. (2005) B-type olivine fabric in the mantle wedge: Insights from high-resolution non-Newtonian subduction zone models. Earth and Planetary Science Letters, 237, 781–797.

Kneller, E.A., Long, M.D. and van Keken, P.E. (2008). Olivine fabric transitions and shear wave anisotropy in the Ryukyu subduction system. Earth and Planetary Science Letters, 268(3–4), 268–282.

Kretz, R. (1966) Interpretation of the Shape of Mineral Grains in Metamorphic Rocks. Journal of Petrology, 7, 68–94.

Laporte, D., and Provost, A. (2000) Equilibrium geometry of a fluid phase in a polycrystalline aggregate with anisotropic surface energies: Dry grain boundaries. Journal of Geophysical Research: Solid Earth, 105, 25937–25953.

Laporte, D., and Watson, E.B. (1995) Experimental and theoretical constraints on melt distribution in crustal sources: the effect of crystalline anisotropy on melt interconnectivity. Chemical Geology, 124.

Laporte, D., Rapaille, C., and Provost, A. (1997) Wetting Angles, Equilibrium Melt Geometry, and the Permeability Threshold of Partially Molten Crustal Protoliths pp. 31–54.

Liu, X., and Zhao, D. (2017) P-wave anisotropy, mantle wedge flow and olivine fabrics beneath Japan. Geophysical Journal International, 210, 1410–1431.

Liu, X., Matsukage, K.N., Li, Y., Takahashi, E., Suzuki, T. and Xiong, X. (2018) Aqueous fluid connectivity in subducting oceanic crust at the mantle transition zone conditions. Journal of Geophysical Research: Solid Earth, 123(8), 6562–6573.

Mackenzie, J.K., (1958) Second paper on statistics associated with the random disorientation of cubes. Biometrika, 45(1–2), 229–240.

Marquardt, K., Rohrer, G.S., Morales, L., Rybacki, E., Marquardt, H., and Lin, B. (2015) The most frequent interfaces in olivine aggregates: the GBCD and its importance for grain boundary related processes. Contributions to Mineralogy and Petrology, 170, 1–17.

Marquardt, K., and Faul, U.H. (2018) The structure and composition of olivine grain boundaries: 40 years of studies, status and current developments. Physics and Chemistry of Minerals, 45(2), 139–172.

Médard, E., McCammon, C.A., Barr, J.A., and Grove, T.L. (2008) Oxygen fugacity, temperature reproducibility, and H_2O contents of nominally anhydrous piston-cylinder experiments using graphite capsules. American Mineralogist, 93, 1838–1844.

Mibe, K., Fujii, T., and Yasuda, A. (1998) Connectivity of aqueous fluid in the Earth's upper mantle. Geophysical Research Letters, 25, 1233–1236.

Mibe, K., Fujii, T., and Yasuda, A. (1999) Control of the location of the volcanic front in island arcs by aqueous fluid connectivity in the mantle wedge. Nature, 401, 259–262.

Morawiec, A. (2010) Volume of intersection of two balls in orientation space. Acta Crystallographica Section A: Foundations of Crystallography, 66(6), 717–719.

Park, H.H., and Yoon, D.N. (1985) Effect of dihedral angle on the morphology of grains in a matrix phase. Metallurgical Transactions A, 16, 923–928.

Pommier, A., and Evans, R.L. (2017) Constraints on fluids in subduction zones from electromagnetic data. Geosphere, 13, 1026–1049.

Pommier, A., Kohlstedt, D.L., Hansen, L.N., Mackwell, S., Tasaka, M., Heidelbach, F., and Leinenweber, K. (2018) Transport properties of olivine grain boundaries from electrical conductivity experiments. Contributions to Mineralogy and Petrology, 173, 41.

Price, J.D., Wark, D.A., Watson, E.B., and Smith, A.M. (2006) Grain-scale permeabilities of faceted polycrystalline aggregates. Geofluids, 6, 302–318.

Smith, C. S. (1948) Grains, phases and interfaces. Transactions of the American Institute of Mining and Metallurgical Engineers, 175, 15–51.

Toramaru, A., and Fujii, N. (1986) Connectivity of melt phase in a partially molten peridotite. Journal of Geophysical Research: Solid Earth, 91, 9239–9252.

van Keken, P.E., Hacker, B.R., Syracuse, E.M., and Abers, G.A. (2011) Subduction factory: 4. Depth-dependent flux of H_2O from subducting slabs worldwide. Journal of Geophysical Research, 116, B01401.

von Bargen, N., and Waff, H.S. (1986) Permeabilities, interfacial areas and curvatures of partially molten systems: Results of numerical computations of equilibrium microstructures. Journal of Geophysical Research, 91, 9261.

Waff, H.S., and Faul, U.H. (1992) Effects of crystalline anisotropy on fluid distribution in ultramafic partial melts. Journal of Geophysical Research, 97, 9003.

Wark, D.A., and Watson, E.B. (2000) Effect of grain size on the distribution and transport of deep-seated fluids and melts. Geophysical Research Letters, 27, 2029–2032.

Watson, E.B., and Brenan, J.M. (1987) Fluids in the lithosphere, 1. Experimentally-determined wetting characteristics of CO_2–H_2O fluids and their implications for fluid transport, host-rock physical properties, and fluid inclusion formation. Earth and Planetary Science Letters, 85, 497–515.

Watson, E.B., and Lupulescu, A. (1993) Aqueous fluid connectivity and chemical transport in clinopyroxene-rich rocks. Earth and Planetary Science Letters, 117, 279–294.

Watson, E.B. (1999) Lithogic partitioning of fluids and melts. American Mineralogist, 84, 1693–1710.

Watson, G.W., Oliver, P.M., and Parker, S.C. (1997) Computer simulation of the structure and stability of forsterite surfaces. Physics and Chemistry of Minerals, 25, 70–78.

Worzewski, T., Jegen, M., Kopp, H., Brasse, H., and Taylor Castillo, W. (2011) Magnetotelluric image of the fluid cycle in the Costa Rican subduction zone. Nature Geoscience, 4, 108–111.

Yoshino, T., Takei, Y., Wark, D.A., and Watson, E.B. (2005) Grain boundary wetness of texturally equilibrated rocks, with implications for seismic properties of the upper mantle. Journal of Geophysical Research: Solid Earth, 110, 1–16.

Yoshino, T., Price, J.D., Wark, D.A., and Watson, E.B. (2006) Effect of faceting on pore geometry in texturally equilibrated rocks: implications for low permeability at low porosity. Contributions to Mineralogy and Petrology, 152, 169–186.

Zheng, Y.F., Chen, R.X., Xu, Z., and Zhang, S.B. (2016) The transport of water in subduction zones. Science China Earth Sciences, 59(4), 651–682.

Figure captions

Figure 1. Representative scanning electron microscope (SEM) images and normalized grain size distribution of run products. a Backscattered electron (BSE) image of the run product in the olivine–H_2O system at 1000°C and 1 GPa for 120 h. **b** High-magnification secondary electron (SE) image of a typical triple junction in the olivine–H_2O system at 1000°C and 1 GPa 120 h, which shows apparent FF angles. **c** Backscattered electron (BSE) image of the run product in the H_2O–CO_2 system ($X_{(CO2)}$ = 0.5) at 1000°C and 1 GPa for 211 h. **d** High-magnification secondary electron (SE) image of the typical apparent θ in the H_2O–CO_2 system ($X_{(CO2)}$ = 0.5) at 1000°C and 1 GPa for 211 h, which shows the coexistence of three types of apparent θ. **e** Backscattered electron (BSE) image of the run product in the H_2O–NaCl system (salinity = 27.5 wt.%) at 2 GPa and 1000°C for 120 h. **f** High-magnification secondary electron (SE) image of typical apparent θ in the H_2O–NaCl system (salinity = 27.5 wt.%) at 2 GPa and 1000°C for 120 h. The run products are composed of mineral grains and epoxy resin-filled pores previously filled with aqueous fluids during the experiment. Orange marks denote olivine–olivine–olivine triple junctions with intersection angles of approximately 120°, indicating the attainment of textural equilibrium. White single and double arrows represent curved and faceted interfaces, respectively. For the CC, FC, and FF angles, the interfaces in **b**, **d**, and **f** are highlighted by cyan curves. Green and red rectangles illustrate suitable and unsuitable angles (i.e., with a crack) for measurement, respectively. **g** Histogram of normalized grain size distribution in the H_2O system at 1 GPa and 1000°C. **h** Histogram of normalized grain size distribution in the H_2O–NaCl system (salinity = 27.5 wt.%) at 2 GPa and 1000°C. The grain size distribution was normalized by the mean grain size of the recovered sample. The grain size peak is concentrated around the

mean grain size. The mean grain size and measured grain number are shown in the panel. Abbreviations: ol = olivine, FF = faceted–faceted angle, FC = faceted–curved angle, CC= curved–curved angle.

Figure 2. Faceting-bearing angle proportion in the olivine–fluid system. Results are calculated from 19 run products with a 10.0 vol.% fluid fraction. The average of 19 values is shown in the panel. The analytical error of each value is 0.5%. The P–T condition and fluid composition for each sample are shown in the panel.

Figure 3. Representative cumulative frequency curves of measured apparent dihedral angles (θ) in the olivine–fluid system at 2 GPa and 800–1000 °C. P–T conditions and fluid composition are shown at the top of each panel. Facet-bearing angles (FC and FF) were measured in this study, while data for the CC angles are from Huang et al. (2019, 2020). The median angle value and number (N) of the measured angles are shown for each case. Thin, solid curves represent theoretical cumulative frequency curves obtained from the isotropic system with one true θ. Abbreviations: FF = faceted–faceted angle, FC = faceted–curved angle, CC = curved–curved angle.

Figure 4. Faceting dependence of median dihedral angles (θ) in the olivine–fluid system at 1–3 GPa and 800–1100 °C. Colors in each panel denote fluid compositions. CC data are from Huang et al. (2019, 2020). An error bar of ± 1.5° is shown in the panels. Abbreviations: FF = faceted–faceted angle, FC = faceted–curved angle, CC = curved–curved angle, I = independent angle type, D = dependent angle type.

Figure 5. Pressure and temperature dependence of median dihedral angles (θ) in the olivine–fluid system. a–f Pressure dependence at 800–1000 °C. **g–i**. Temperature dependence at 2 GPa. P–T conditions and fluid composition are shown in each panel. CC data are from Huang et al. (2019). An error bar of ± 1.5° is shown along with the median angle. The blue dash line represents θ of 60°. Abbreviations: FF = faceted–faceted angle, FC = faceted–curved angle, CC = curved–curved angle.

Figure 6. Representative EBSD maps and corresponding pole figures. a1–e1 Raw EBSD maps of recovered olivine aggregate in olivine–fluid systems. Small points within grains are attributed to noise, crystal defects, and fluid inclusions. **a2–e2** Denoised EBSD maps of recovered olivine aggregate in olivine–fluid systems. Points smaller than 1 μm have been removed. **a3–e3** Pole figures showing the crystallographic orientations of (100), (010), and (001) corresponding to **a2–e2**. Intensities in the color bar are multiples of the uniform distribution (MUD). All grains defined by different colors are olivine with different orientations. P–T conditions and fluid composition are shown at the top of **a–e**. The arrow on the left represents the compaction direction (parallel to the direction of piston movement).

Figure 7. Olivine grains' representative 3D crystal orientation and corresponding secondary electron image in the olivine–fluid system. Raw EBSD maps in the H_2O system at 1 GPa and 1000°C **(a1)**, in the H_2O–CO_2($X_{(CO2)}$=0.5) system at 1 GPa and 1000°C **(b1)**, in the H_2O system at 2 GPa and 1000°C **(c1)**, and in the H_2O–NaCl (27.5 wt.%) system at 2 GPa and 1000°C **(d1)**. **a2–d2**, Denoised EBSD maps with 3D crystal orientations of olivine corresponding to **a1–d1.** Colored areas denote olivine grains with different orientations, and white areas represent noise, defects, fluid inclusions, and fluid pools. The 3D crystal

orientation was visualized for each grain in the high magnification images by showing the oriented olivine crystal with an idealized morphology. Even though the grain configurations in **a2–d2** were slightly altered during EBSD data processes (MTEX MATLAB toolbox) such as denoising and binarization, this essentially has no effect on orientation identification. **a3–d3** Secondary electron (SE) images of recovered olivine aggregates corresponding to **a1–d1**. Olivine grains have a grey color; fluid pools are black areas that are sometimes filled by resin. An orange outline visually emphasizes the interface between the olivine and fluids, and apparent angles with a sequenced number are examples of analyzed angles and corresponding grain boundaries. **a4–d4** Dihedral angle types, and their values in terms of FF, FC, and CC corresponding to measured angles in **a3–d3**. These angles have values close to the corresponding median θ. **e** Crystal habit of a single olivine crystal derived using the MTEX MATLAB toolbox. The blue squares in a3, c3, and d3 represent θ that has one shared flat plane for both the grain boundary and interfacial boundary. The white circles in b3 and d3 represent the angle defined by interfaces of one grain/sub-grain, which was not included in our discussion. Abbreviations: ol = olivine, FF = faceted–faceted angle, FC = faceted–curved angle, CC = curved–curved angle.

Figure 8. Pole figure of grain boundary plane distribution. a1–a3 Grain boundary plane distribution (GBPD) in the I group (i.e., systems where θ values are independent of angle type). **b1–b3** Grain boundary plane distribution (GBPD) in the D group (i.e., systems where faceting increases θ). The equivalent olivine orientations obtained in the analysis were rearranged into the first quadrant to better highlight the results. Subsequently, by assuming that the grain boundary planes were equally distributed in each quadrant, the orientations in the first quadrant were copied in the other quadrants to obtain the pole figure. The analyzed

number (N) in the first quadrant is shown at the lower left in each pole figure. MUD is the multiples of uniform density, shown by the color bar's intensities. The Miller indices were marked around the high MUD. The assumed error is ±20°. Abbreviations: FF = faceted–faceted angle, FC = faceted–curved angle, CC = curved–curved angle, I = independent angle type, D = dependent angle type.

Figure 9. Pole figure of FC angles. Pole figure of grain boundary plane distributions (GBPDs) of faceted (**a2–1** and **b2–1**) and curved (**a2–2** and **b2–2**) sides at the FC triple junction for the I group (i.e., the systems where the θ values are independent of the angle type; **a2–1** and **a2–2**) and D group (i.e., the systems where the faceting increases θ; **b2–1** and **b2–2**). The data were plotted in the same way as in Figure 8. The analyzed number (N) in the first quadrant is shown at the lower left in each pole figure. MUD represents the multiples of uniform density, which shows the intensities in the color bar. The Miller indices were marked around the high MUD. The assumed error is ± 20°. Abbreviations: FC = faceted–curved angle, F = grain boundary at the faceting side, C = grain boundary at the curved side, I = angle type independent group, D = angle type dependent group.

Figure 10. Distribution of misorientation angles. The misorientation angle between each pair of two measured olivine grains was calculated based on the Euler angle derived from EBSD. **a** Misorientation angle of the FF type angle. **b** Misorientation angle of the FC type angle. **c** Misorientation angle of the CC type angle. The red curve represents the theoretical random distribution of olivine grains. The number of angles (N) is shown in the panel.

Figure 11. Misorientation axis distribution. All axes of measured grain pairs were mapped into a unit quadrant owing to symmetry equivalence. **a** All misorientation axis of the FF type

angle. **b** All misorientation axis of the FC type angle. **c** All misorientation axis of the CC type angle. **d** Theoretical misorientation axis distribution for a perfectly random polycrystal based on the analytical solution (Mackenzie 1958). The number of angles (N) is shown in the panel. The scale is in units of multiples of uniform distribution (MUD). The highest MUD is the most frequent axis (121).

Figure 12. Random test of the DCC dataset (b3 in Figure 8). a Test repeated 10 times with 50 randomly selected measurements. **b** Test repeated 10 times with 75 randomly selected measurements. **c** Test repeated 10 times with 125 randomly selected measurements. The number of random selections (RN) is shown for each series of tests. The scale is in units of multiples of uniform distribution (MUD). The assumed error is ± 20°.

Supplementary figure captions

Figure S1. Histogram of normalized grain size distribution in the olivine–fluid system. The grain size distribution was normalized by the mean grain size of the recovered sample. The grain size peak is concentrated around the mean grain size. The mean grain size and measured grain number are shown in the panel. Abbreviation: ol = olivine.

Figure S2. Cumulative frequency curves of measured apparent dihedral angles (θ) in olivine–fluid systems at 1–3 GPa and 800–1100 °C. The median value and number (N) of the measured angles are shown for each experimental condition. The solid lines represent the theoretical cumulative frequency curves of the isotropic system with one true θ (Jurewicz and Jurewicz 1986). This angle is assumed to coincide with the obtained median value. P–T conditions and fluid composition are shown for each system. Abbreviations: ol=olivine, FFT

= faceted–faceted angle, FCT = faceted–curved angle, CCT= curved–curved angle, AllT= all types of measured angle.

Figure S3. Frequency distribution histograms of measured apparent dihedral angles (θ) in olivine–fluid systems at 1–3 GPa and 800–1100 °C. Theoretical distributions (orange curves) for mono–mineral and isotropic systems are also shown in the histograms along with the median values (Jurewicz and Jurewicz 1986). The P–T and fluid composition are shown for each system. Abbreviations: ol=olivine, FFT = faceted–faceted angle, FCT = faceted–curved angle, CCT= curved–curved angle, AllT= all types of measured angle.

Figure S4. EBSD maps and corresponding pole figures under static compression conditions. a1–e1 Raw EBSD maps of recovered olivine aggregate in olivine–fluid systems. Small points within grains are attributed to noise, crystal defects, and fluid inclusions. **a2–e2** Denoised EBSD maps corresponding to **a1–e1**. Points smaller than 1 μm have been removed. All grains defined by different colors are olivine with different orientations. **a3–e3** Pole figures showing the crystallographic orientation of (100), (010), and (001) corresponding to **a2–e2**. Color intensities are multiples of the random distribution (MUD). P–T conditions and fluid composition are shown along with the corresponding system. Abbreviation: ol=olivine.

Figure S5. Schematic olivine–olivine–fluid triple junction with a sectioning plane after Harker and Parker (1945) and Jurewicz and Jurewicz (1986). True dihedral angle (θ) formed by two olivine–fluid interfaces (pale blue planes). Y is the apparent dihedral angle observed on the sectioning plane (pale orange plane). The bold red line represents the unit normal of the sectioning plane defined in the angular coordinates Q and ϕ. F is the angle formed by the sectioning plane and grain boundary plane (deep sky blue plane).

DOI: https://doi.org/10.2138/am-2022-8808. http://www.minsocam.org/

Figure S6. Sectioning calculation at the olivine–olivine–fluid triple junction. a Contours of the apparent dihedral angle, Y in the sin^{2}Q versus ϕ diagram calculated according to Harker and Parker (1945) assuming a true dihedral angle, θ of 60°. **b** Contours of the angle formed by the grain boundary plane and sectioning plane, F, in the sin^{2}Q versus ϕ diagram. **c** Area of F ≥ 67° within the Y window of 0°–65° in the sin^{2}Q versus ϕ diagram (orange). The ratio of this area to the area of Y = 0°–60° (orange + pale yellow) yields the probability of F ≥ 67° in the selected Y window.

Figure S7. Random test of the DCC dataset (b3 in Figure 8). a Test repeated 10 times with 25 randomly selected measurements. **b** Test repeated 10 times with 100 randomly selected measurements. **c** Test repeated 10 times with 150 randomly selected measurements. The number of random selections (RN) is shown for each series of tests. The scale is in units of multiples of uniform distribution (MUD). The assumed error is ± 20°.

Supplementary Information

Supplementary Note 1. Errors in GBPD analyses

Our GBPD analyses focused on the olivine–olivine–fluid triple junction with apparent dihedral angles lower than the median value + 5° and assumed a vertical grain boundary plane. Based on a simple theoretical calculation, we show that grain boundary planes at such triple junctions are dominantly subvertical with respect to the polished section. Although we cannot exactly determine the extent of grain boundary plane tilting in cross-sectional images, the apparent dihedral angles can be used to constrain the extent of tilting statistically.

DOI: https://doi.org/10.2138/am-2022-8808. http://www.minsocam.org/

Following the method of Harker and Parker (1945), we can calculate the apparent dihedral angle, Y on an arbitrary sectioning plane at the mineral–mineral–fluid triple junction in an isotropic system, with one true dihedral angle θ. This method is identical to that used to compute the theoretical cumulative frequency curve of the apparent dihedral angle, as shown in Figure 3. A schematic of the triple junction with a sectioning plane is shown in Figure S5. The unit normal of the sectioning plane is defined in angular coordinates Q and ϕ (Q, ϕ = 0°–90°), and Y is a function of θ, Q, and ϕ (Harker and Parker 1945). In Figure S6a, the contours of Y for a representative θ of 60° are shown in the $\sin^2 Q$ versus ϕ diagram. In this diagram, the area fraction of angles ≤ Y corresponds to the probability that the observed apparent dihedral angles become ≤ Y (Harker and Parker 1945). The apparent dihedral angles around θ were more likely to be observed on the polished section than the other angles. The median of the Y values closely corresponds to θ (Jurewicz and Jurewicz 1986). We noted that a Y value smaller than θ required a smaller ϕ, and vice versa. Increasing $\sin^2 Q$ (i.e., Q) tended to cause Y values to deviate from the median (i.e., θ).

The angle between the grain boundary plane and the arbitrary sectioning plane, F (F = 0°–90°) can be calculated from their normals. F is dependent on Q and ϕ, but independent of θ (Figure S1). In Figure S6b, the contours of F are shown in the $\sin^2 Q$ versus ϕ diagram. As in the case of Y, the area fraction of angles of ≥ F should correspond to the probability that the angles become ≥ F. At $\sin^2 Q$ (i.e., Q) = 0 or ϕ = 0, the grain boundary plane is vertical (F = 90°). With increasing Q and ϕ, F tends to deviate from 90°; that is, the grain boundary plane becomes tilted. Therefore, subvertical (i.e., F close to 90°) grain boundary planes can be expected at triple junctions with Y smaller than the median, because such Y values can only be observed at low ϕ.

DOI: https://doi.org/10.2138/am-2022-8808. http://www.minsocam.org/

Combining the Y and F contours in the $\sin^2$Q versus ϕ diagram allows us to compute the probability of observing sub-vertical grain boundary planes at triple junctions in an arbitrary Y window on the polished section. We regarded the minimum deviation of F from 90°, which satisfies probability of more than approximately 68%, as the representative error (1s) of our GBPD analyses. In Figure S6c, the area of F ≥ 67° in our preferred Y window from 0° to 65° (i.e., median + 5°) is shown in the $\sin^2$Q versus ϕ diagram for θ = 60°. We found that 71% of the apparent dihedral angles fell within the range of 0° ≤ Y ≤ 65°, in which 68% of grain boundary planes formed an angle ≥ 67° with respect to the sectioning plane. Thus, we inferred a representative error of approximately 23° in our GBPD analyses. Although this value slightly increased and decreased at lower and higher θ, respectively, it was not significantly dependent on θ in the range of interest (23°–24° at θ = 50°–80°). If we do not use dihedral angle constraints (i.e., a Y window of 0°–180°), the probability of F ≥ 67° decreases to 49% and the estimated error becomes 35°.

References

Harker, D., and Parker, E.R. (1945) Grain shape and grain growth. Transactions of the American Society for Metals, 34, 156–201.

Jurewicz, S.R., and Jurewicz, A.J.G. (1986) Distribution of apparent angles on random sections with emphasis on dihedral angle measurements. Journal of Geophysical Research, 91, 9277.

Tables

Table 1. Experimental conditions and results

Run no.	P (GPa)	T (°C)	Duration (h)	Fluid phase	Salinity (wt%)	$X(CO_2)$	Statistic angle number for faceting ratio	Faceting proportion (%)	EBSD	GBPD	Angle Type	Number of angle measured	Median (Degree)	I&D group
1	1	800	192	H_2O	0	-	187	32.6	-	-	FF	112	70.8	I
											FC	174	70.4	
											CC[a]	200	71.2	
											All	486	71.0	
2	1	800	192	H_2O-NaCl	5	-	218	31.9	-	-	FF	137	68.4	D
											FC	176	63.1	
											CC[a]	222	58.5	
											All	535	62.0	
3	1	800	192	H_2O-NaCl	27.5	-	309	32.9	-	-	FF	120	66.3	D
											FC	126	62.3	
											CC[a]	207	58.3	
											All	453	60.6	
4	1	1000	120	H_2O	0	-	509	30.4	√	√	FF	134	63.6	I
											FC	143	64.2	
											CC[a]	210	64.1	
											All	487	63.8	
5	1	1000	120	H_2O-CO_2	0	0.5	383	32.1	√	√	FF	148	79.2	I
											FC	171	78.4	
											CC[b]	213	78.2	
											All	532	78.5	
6	1	1000	120	H_2O-NaCl	27.5	-	302	32.0	√	√	FF	115	62.0	D
											FC	174	59.7	
											CC[a]	208	56.1	
											All	497	57.8	
7	2	800	212	H_2O	0	-	205	31.8	√	-	FF	136	68.7	I
											FC	178	68.8	
											CC[a]	212	69.9	
											All	526	69.1	
8	2	800	192	H_2O-NaCl	5	-	201	33.3	√	√	FF	118	64.3	D
											FC	172	57.9	
											CC[a]	247	53.6	
											All	537	56.4	
9	2	800	210	H_2O-NaCl	27.5	-	269	31.3	√	√	FF	107	66.5	D
											FC	178	59.0	
											CC[a]	210	56.4	
											All	495	59.0	
10	2	1000	120	H_2O	0	-	582	33.5	√	√	FF	102	58.4	I
											FC	249	57.5	
											CC[a]	213	58.0	
											All	564	57.8	
11	2	1000	133	H_2O-NaCl	5	-	314	32.8	√	√	FF	101	50.7	D
											FC	188	46.5	
											CC[a]	201	43.4	
											All	490	45.0	
12	2	1000	120	H_2O-NaCl	27.5	-	136	33.8	√	√	FF	120	57.0	D
											FC	159	55.6	
											CC[a]	304	51.7	
											All	583	53.7	
13	2	1100	72	H_2O	0	-	284	34.2	-	-	FF	134	59.1	D
											FC	153	56.9	
											CC[a]	210	53.8	
											All	497	55.9	
14	2	1100	72	H_2O-NaCl	27.5	-	201	30.0	-	-	FF	104	58.3	D
											FC	224	52.6	
											CC[a]	202	47.1	
											All	530	50.2	
15	3	800	211	H_2O	0	-	100	35.8	-	-	FF	123	64.9	I
											FC	135	65.0	
											CC[a]	200	66.2	
											All	458	66.0	
16	3	800	192	H_2O-NaCl	5	-	166	33.6	-	-	FF	107	55.0	D
											FC	132	53.2	
											CC[a]	242	50.2	
											All	481	52.4	
17	3	800	211	H_2O-NaCl	27.5	-	157	36.9	-	-	FF	103	64.0	D
											FC	164	60.2	
											CC[a]	200	56.4	
											All	467	60.0	
18	3	1000	120	H_2O	0	-	344	28.3	-	-	FF	110	60.6	D
											FC	199	54.7	
											CC[a]	205	49.2	
											All	514	53.7	
19	3	1000	120	H_2O-NaCl	27.5	-	158	30.0	√	√	FF	102	61.4	D
											FC	147	55.5	
											CC[a]	220	47.4	
											All	469	51.6	

Note: The fluid fraction in each experiment was ~10.0 vol.%. The true θ value for each system was a median value ± 1.5°. The analytical error for the faceting proportion was 0.5%. **a** the CC angle data is cited from Huang et al. (2019); **b** the CC angle data is cited from Huang et al. (2020). The run products that were employed for the electron backscattered diffraction (EBSD) and grain boundary plane distribution (GBPD) are marked in the table. $X_{(CO2)}$ = $CO_2/(H_2O+CO_2)$ in mole. Abbreviations: ol = olivine, FF = faceted–faceted angle, FC = faceted–curved angle, CC = curved–curved angle, All = all measured angles, I = angle type independent, D = angle type dependent.

Table 2. Theoretical FF angle between two crystal planes

Crystal	GBCP	IBCP	ACP(°)	Calculated FF Angle(°)	Configuration	Measured FF angle(°)
C1	101	001	51.5	51.5	Flat face	50–55
C1	101	120	55.1	55.1	Flat face	
C1 C2	100 100	110 101	25.0 38.5	63.5	Asymmetrical	55–65
C1 C2	100 010	110 021	25.0 40.7	65.7	Asymmetrical	65–70
C1	101	021	66.2	66.2	Flat face	
C1 C2	100 100	110 120	25.0 43.0	68.0	Asymmetrical	
C1 C2	100 101	110 110	25.0 44.8	69.8	Asymmetrical	
C1 C2	100 101	110 001	25.0 51.5	76.5	Asymmetrical	75–80
C1 C2	100 010	101 021	38.5 40.7	79.2	Asymmetrical	
C1 C2	100 101	110 120	25.0 55.1	80.1	Asymmetrical	
C1 C2	100 100	101 120	38.5 43.0	81.5	Asymmetrical	

Note: The calculated FF angle was obtained by summing the two angles between two crystal planes (ACP). This configuration shows the geometry of the calculated dihedral angle. We assume that the two crystals (crystal 1, C1; crystal 2, C2) are touching with different (i.e., asymmetrical configuration) low–Miller index planes to form the FF angle. Additionally, we show extreme cases where one flat plane is shared for both grain boundary and interfacial boundary (i.e., flat face). GBCP, grain boundary crystal plane; IBCP, interfacial boundary crystal plane. The crystal cell parameters (a=4.7540 Å, b=10.1971 Å, and c=5.9806 Å) employed for the angle calculation were cited from Deer et al. (2013).

Supplementary Table

Table S1. List of calculated FF–type dihedral angles formed by low–Miller Index grain boundary planes and interfaces with fluid at a triple junction

Grain Boundary Plane	Faceted Interface	C1 \ C2	*25.0*	*43.0*	*38.5*	*47.0*	*40.7*	*66.2*	*55.1*	*51.5*	*44.8*	Flat face
100	110	*25.0*	**50.0**	68.0	63.5	72.0	65.7	91.2	80.1	76.5	69.8	25.0
100	120	*43.0*	68.0*	**86.0**	81.5	90.0	83.7	109.2	98.1	94.5	87.8	43.0
100	101	*38.5*	63.5*	81.5*	**77.0**	85.5	79.2	104.7	93.6	90.0	83.3	38.5
010	120	*47.0*	72.0	90.0	85.5	**94.0**	87.7	113.2	102.1	98.5	91.8	47.0
010	021	*40.7*	65.7*	83.7	79.2*	87.7	**81.4**	106.9	95.8	92.2	85.5	40.7
101	021	*66.2*	91.2	109.2	104.7	113.2	106.9	**132.4**	121.3	117.7	111	66.2*
101	120	*55.1*	80.1*	98.1	93.6	102.1	95.8	121.3	**110.2**	106.6	99.9	55.1*
101	001	*51.5*	76.5*	94.5	90.0	98.5	92.2	117.7	106.6	**103**	96.3	51.5*
101	110	*44.8*	69.8*	87.8	83.3	91.8	85.5	111.0	99.9	96.3	**89.6**	44.8

Note: Bold represents symmetric configuration, which are not dihedral angles because a grain boundary cannot be defined between the two adjacent grains with the same crystallographic orientation (i.e., symmetrical configurations). The star superscript represents calculated angles that are consistent with experimental data.

Figures

Figure 1

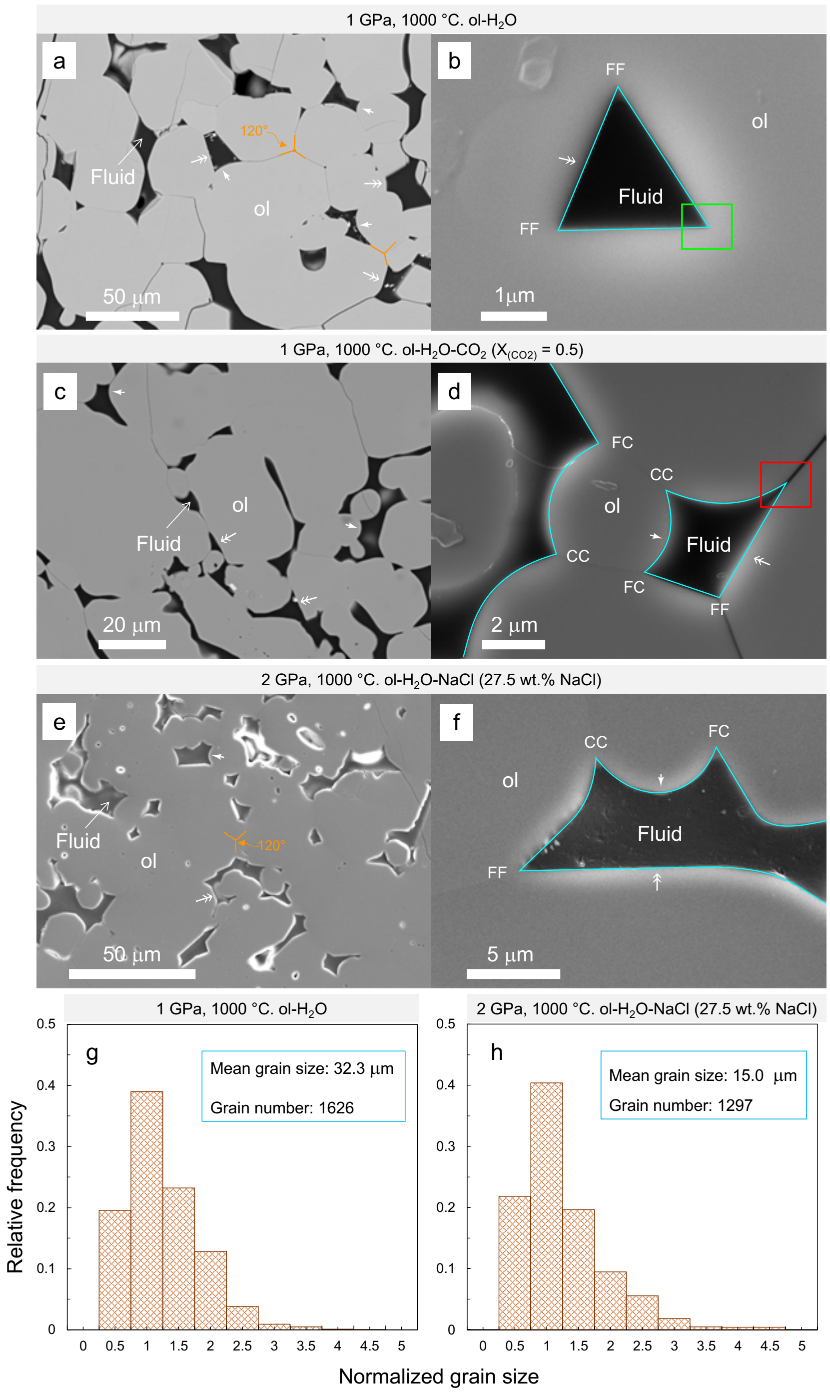

Figure 2

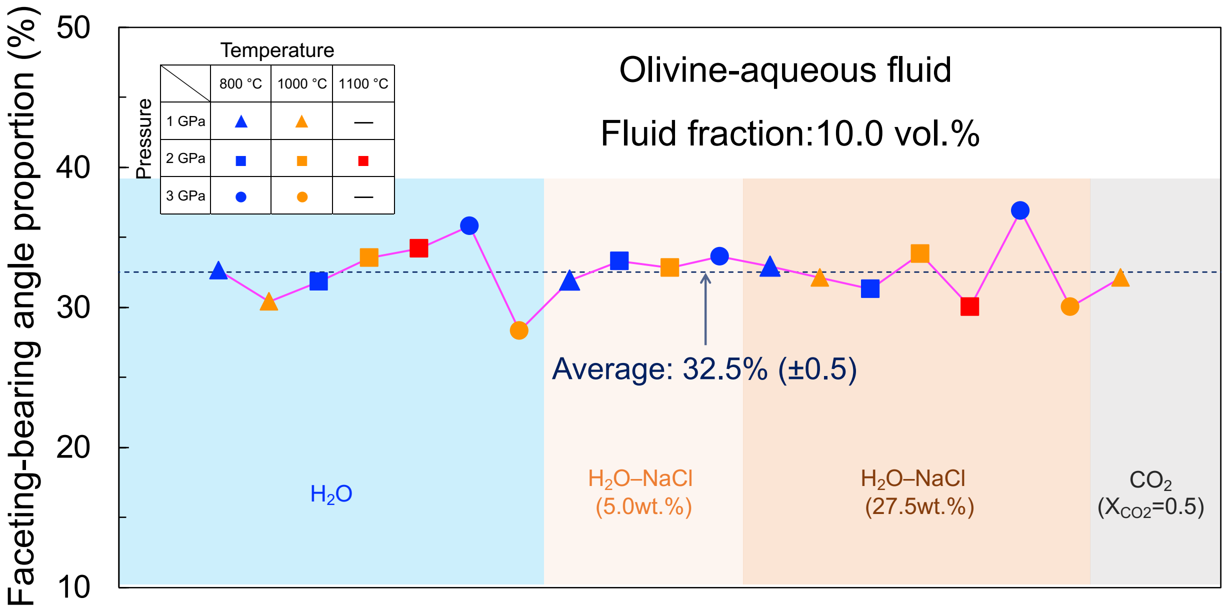
Olivine-aqueous fluid
Fluid fraction:10.0 vol.%
Temperature
800 °C
1000 °C
1100 °C
Pressure
1 GPa
2 GPa
3 GPa
Faceting-bearing angle proportion (%)
50
40
30
20
10
Average: 32.5% (±0.5)
H_2O
H_2O–NaCl (5.0wt.%)
H_2O–NaCl (27.5wt.%)
CO_2 (X_{CO2}=0.5)

Figure 3

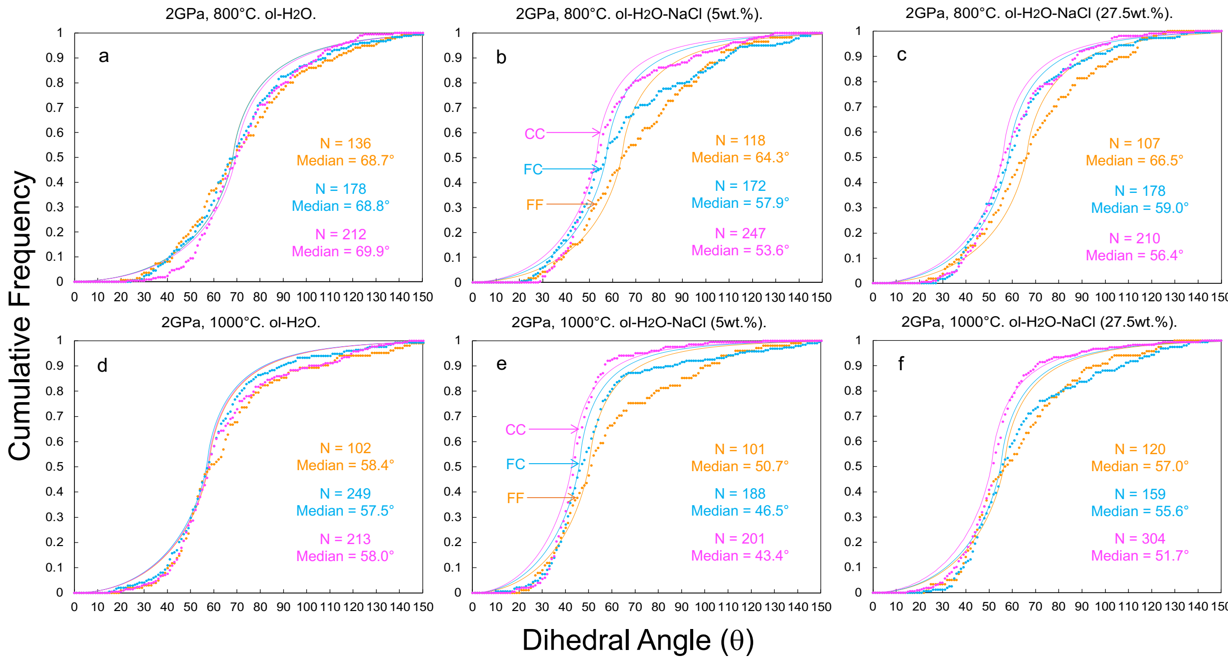

2GPa, 800°C. ol-H2O.
2GPa, 800°C. ol-H2O-NaCl (5wt.%).
2GPa, 800°C. ol-H2O-NaCl (27.5wt.%).
2GPa, 1000°C. ol-H2O.
2GPa, 1000°C. ol-H2O-NaCl (5wt.%).
2GPa, 1000°C. ol-H2O-NaCl (27.5wt.%).
a
N = 136
Median = 68.7°
N = 178
Median = 68.8°
N = 212
Median = 69.9°
b
CC
FC
FF
N = 118
Median = 64.3°
N = 172
Median = 57.9°
N = 247
Median = 53.6°
c
N = 107
Median = 66.5°
N = 178
Median = 59.0°
N = 210
Median = 56.4°
d
N = 102
Median = 58.4°
N = 249
Median = 57.5°
N = 213
Median = 58.0°
e
CC
FC
FF
N = 101
Median = 50.7°
N = 188
Median = 46.5°
N = 201
Median = 43.4°
f
N = 120
Median = 57.0°
N = 159
Median = 55.6°
N = 304
Median = 51.7°
Cumulative Frequency
Dihedral Angle (θ)

Figure 4

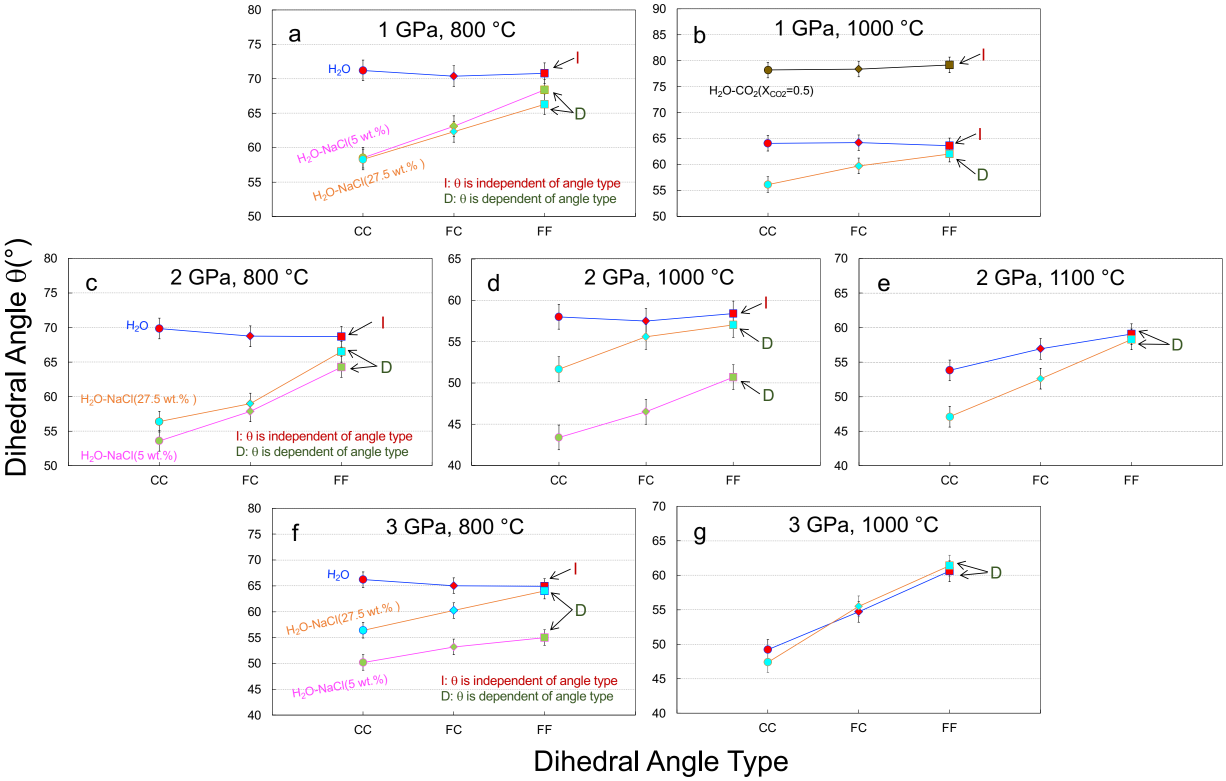

a
1 GPa, 800 °C
H2O
H2O-NaCl(5 wt.%)
H2O-NaCl(27.5 wt.%)
I: θ is independent of angle type
D: θ is dependent of angle type
b
1 GPa, 1000 °C
H2O-CO2(XCO2=0.5)
c
2 GPa, 800 °C
d
2 GPa, 1000 °C
e
2 GPa, 1100 °C
f
3 GPa, 800 °C
g
3 GPa, 1000 °C
CC
FC
FF
I
D
Dihedral Angle θ(°)
Dihedral Angle Type

Figure 5

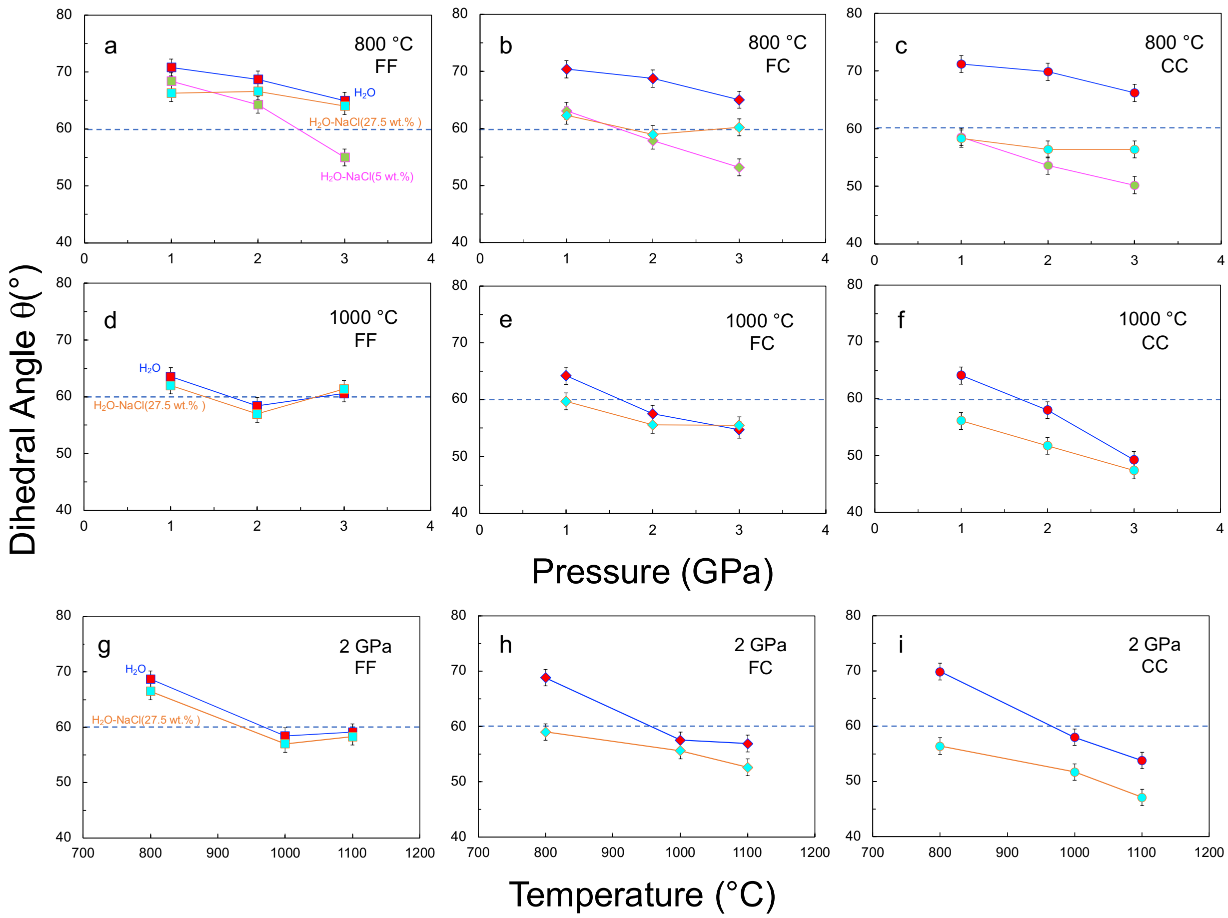
a
800 °C
FF
H_2O
H_2O-NaCl(27.5 wt.%)
H_2O-NaCl(5 wt.%)
b
800 °C
FC
c
800 °C
CC
d
1000 °C
FF
e
1000 °C
FC
f
1000 °C
CC
g
2 GPa
FF
h
2 GPa
FC
i
2 GPa
CC
Dihedral Angle θ(°)
Pressure (GPa)
Temperature (°C)

Figure 6

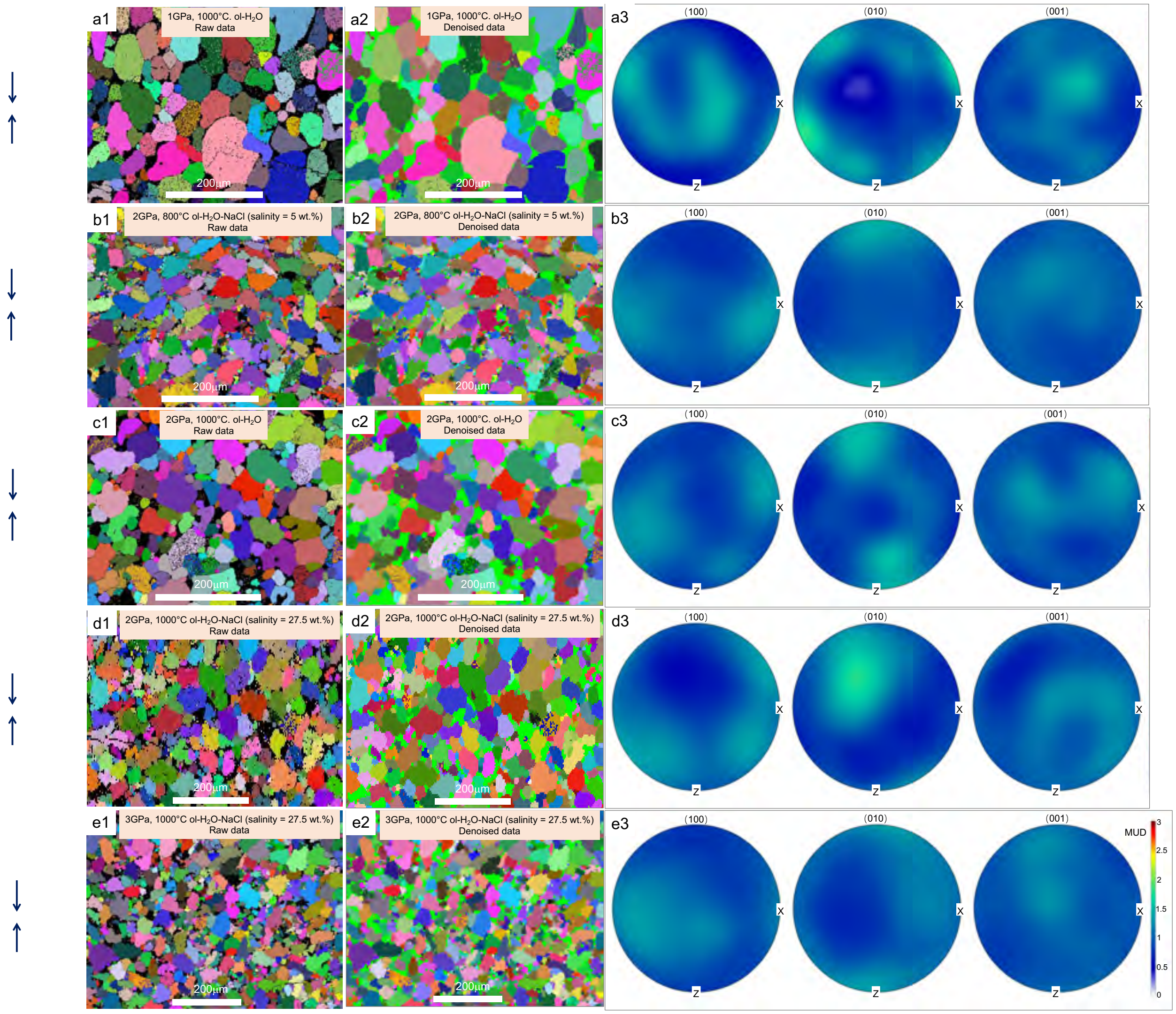
a1
1GPa, 1000°C. ol-H2O
Raw data
200μm
a2
1GPa, 1000°C. ol-H2O
Denoised data
200μm
a3
(100)
(010)
(001)
b1
2GPa, 800°C ol-H2O-NaCl (salinity = 5 wt.%)
Raw data
b2
2GPa, 800°C ol-H2O-NaCl (salinity = 5 wt.%)
Denoised data
b3
c1
2GPa, 1000°C. ol-H2O
Raw data
c2
2GPa, 1000°C. ol-H2O
Denoised data
c3
d1
2GPa, 1000°C ol-H2O-NaCl (salinity = 27.5 wt.%)
Raw data
d2
2GPa, 1000°C ol-H2O-NaCl (salinity = 27.5 wt.%)
Denoised data
d3
e1
3GPa, 1000°C ol-H2O-NaCl (salinity = 27.5 wt.%)
Raw data
e2
3GPa, 1000°C ol-H2O-NaCl (salinity = 27.5 wt.%)
Denoised data
e3
MUD
x
z

Figure 7

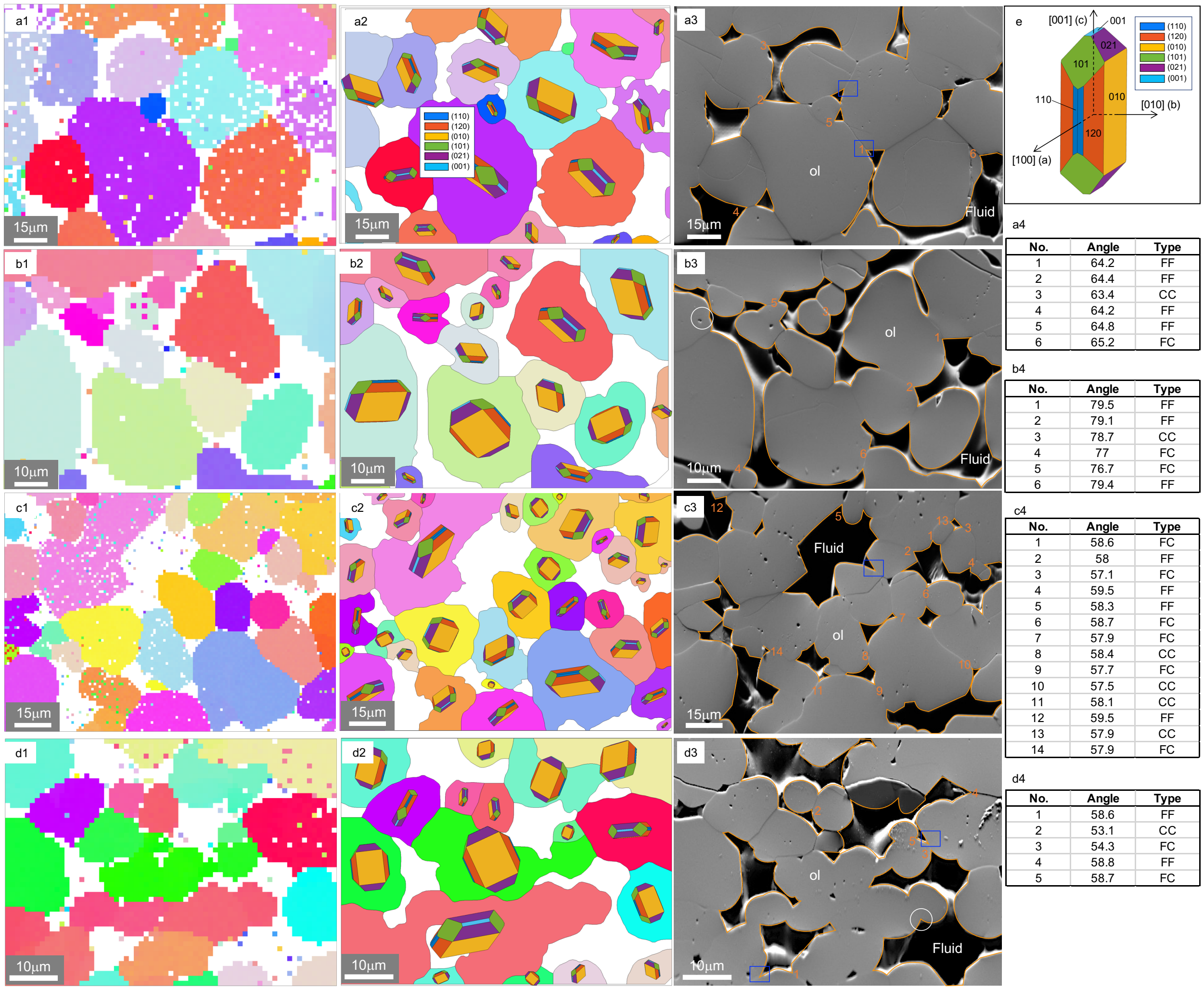

a4

No.	Angle	Type
1	64.2	FF
2	64.4	FF
3	63.4	CC
4	64.2	FF
5	64.8	FF
6	65.2	FC

b4

No.	Angle	Type
1	79.5	FF
2	79.1	FF
3	78.7	CC
4	77	FC
5	76.7	FC
6	79.4	FF

c4

No.	Angle	Type
1	58.6	FC
2	58	FF
3	57.1	FC
4	59.5	FF
5	58.3	FF
6	58.7	FC
7	57.9	FC
8	58.4	CC
9	57.7	FC
10	57.5	CC
11	58.1	CC
12	59.5	FF
13	57.9	CC
14	57.9	FC

d4

No.	Angle	Type
1	58.6	FF
2	53.1	CC
3	54.3	FC
4	58.8	FF
5	58.7	FC

Figure 8

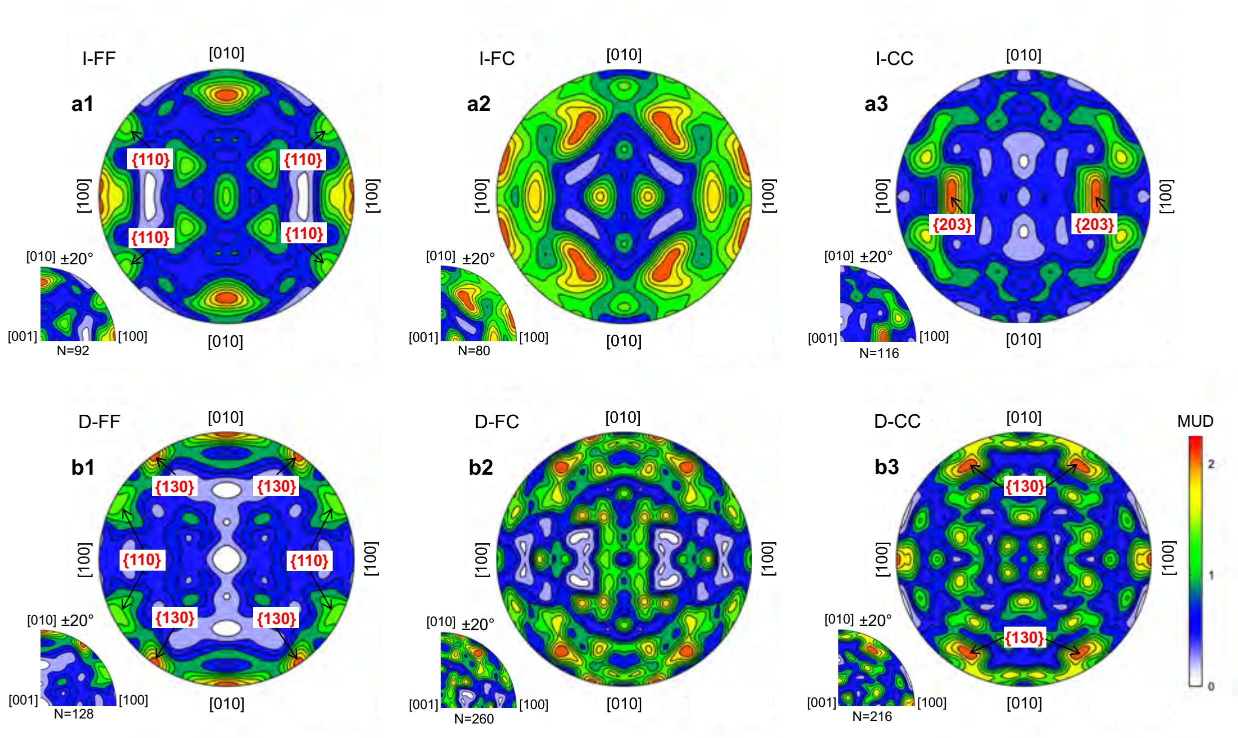

I-FF
a1
[010]
[100]
{110}
{110}
{110}
{110}
[010] ±20°
[001]
[100]
N=92
I-FC
a2
N=80
I-CC
a3
{203}
{203}
N=116
D-FF
b1
{130}
{110}
N=128
D-FC
b2
N=260
D-CC
b3
{130}
N=216
MUD
2
1
0

Figure 9

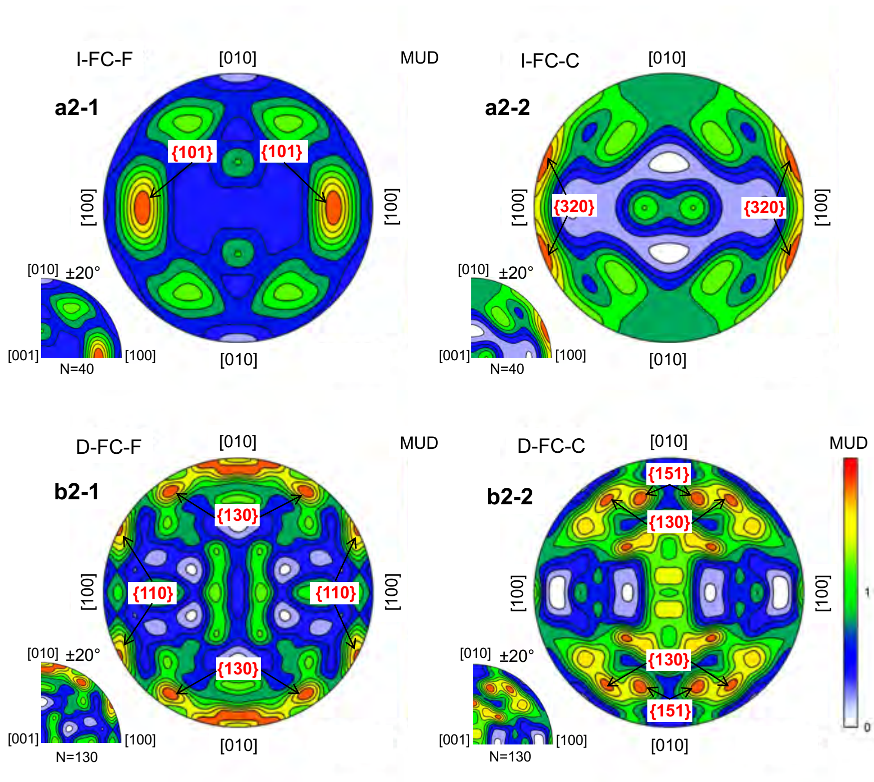
I-FC-F
a2-1
[010]
MUD
{101}
{101}
[100]
[100]
[010] ±20°
[001]
[100]
N=40
[010]
I-FC-C
a2-2
[010]
{320}
{320}
[100]
[100]
[010] ±20°
[001]
[100]
N=40
[010]
D-FC-F
b2-1
[010]
MUD
{130}
{110}
{110}
{130}
[100]
[100]
[010] ±20°
[001]
[100]
N=130
[010]
D-FC-C
b2-2
[010]
{151}
{130}
{130}
{151}
[100]
[100]
[010] ±20°
[001]
[100]
N=130
[010]
MUD
1
0

Figure 10

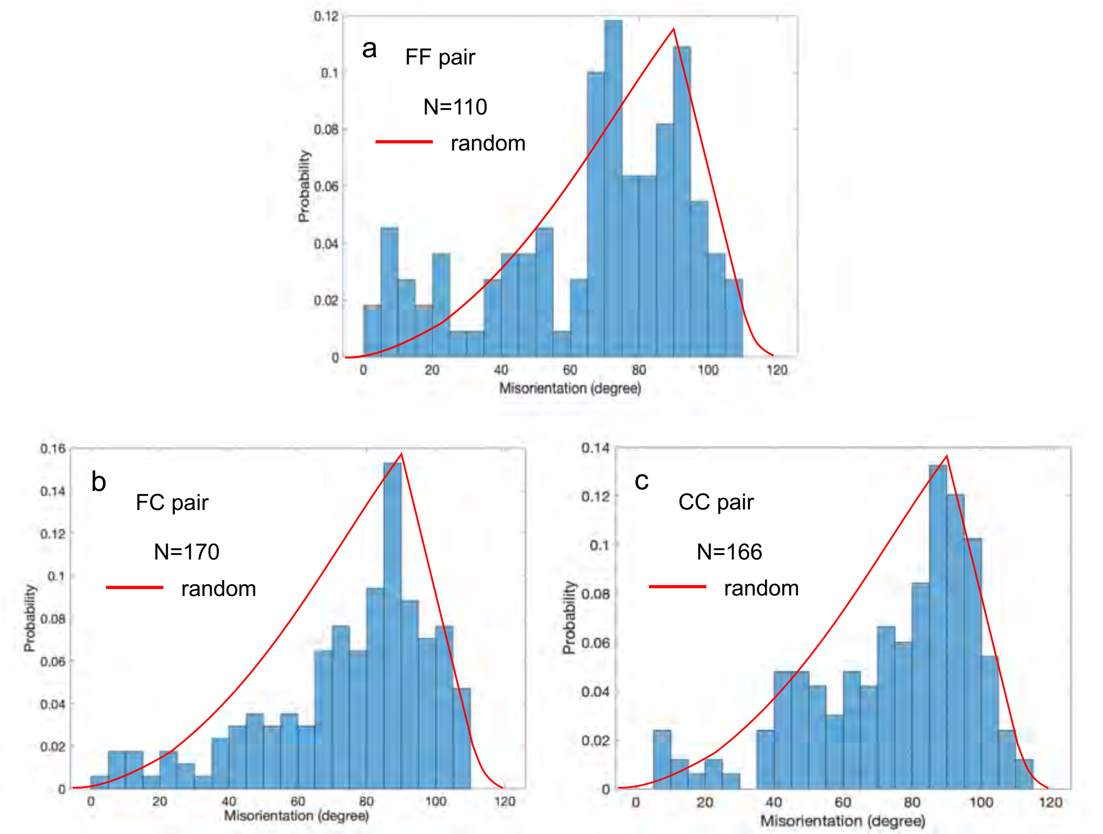
a
FF pair
N=110
random
Probability
Misorientation (degree)
b
FC pair
N=170
random
Probability
Misorientation (degree)
c
CC pair
N=166
random
Probability
Misorientation (degree)

Figure 11

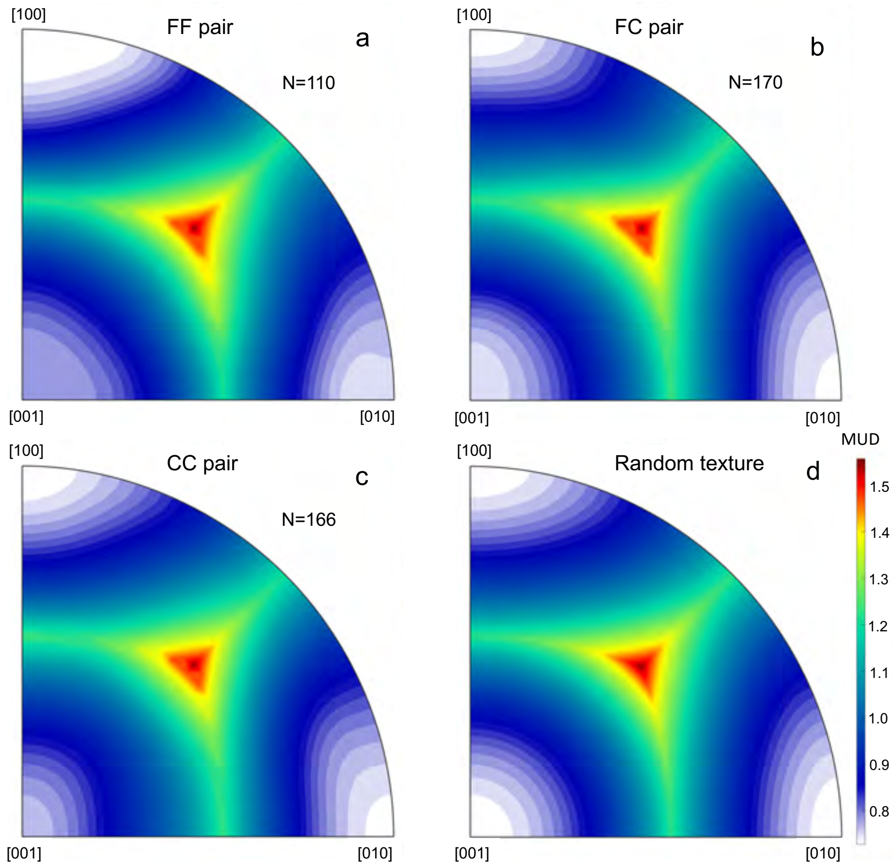
FF pair
a
N=110
[100]
[001]
[010]
FC pair
b
N=170
[100]
[001]
[010]
CC pair
c
N=166
[100]
[001]
[010]
Random texture
d
[100]
[001]
[010]
MUD
1.5
1.4
1.3
1.2
1.1
1.0
0.9
0.8

Figure 12

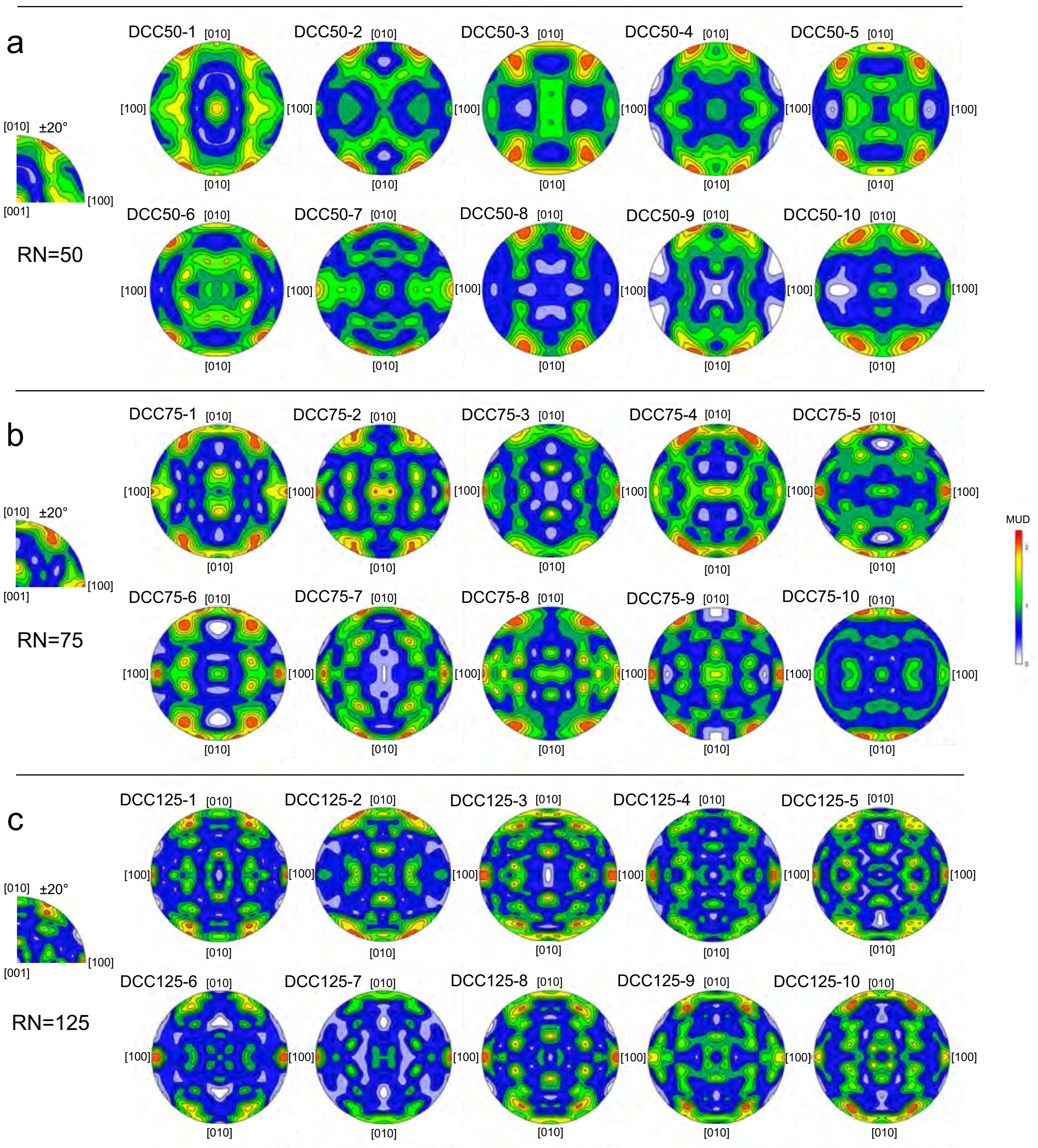

a
RN=50
DCC50-1
DCC50-2
DCC50-3
DCC50-4
DCC50-5
DCC50-6
DCC50-7
DCC50-8
DCC50-9
DCC50-10
b
RN=75
DCC75-1
DCC75-2
DCC75-3
DCC75-4
DCC75-5
DCC75-6
DCC75-7
DCC75-8
DCC75-9
DCC75-10
c
RN=125
DCC125-1
DCC125-2
DCC125-3
DCC125-4
DCC125-5
DCC125-6
DCC125-7
DCC125-8
DCC125-9
DCC125-10
[010]
[100]
[001]
±20°
MUD